ABSTRACT

Title of Dissertation: INTERACTING PHOTONS IN CIRCUIT QUANTUM ELECTRODYNAMICS: DECAY OF THE COLLECTIVE PHASE MODE IN ONE-DIMENSIONAL JOSEPHSON JUNCTION ARRAYS DUE TO QUANTUM PHASE-SLIP FLUCTUATIONS

Nicholas Christopher Grabon
Doctor of Philosophy, 2020

Dissertation Directed by: Professor Vladimir Manucharyan
Department of Physics

Light does not typically scatter light, as witnessed by the linearity of Maxwell's equations. In this work, we demonstrate two superconducting circuits, in which microwave photons have well-defined energy and momentum, but their lifetime is finite due to decay into lower energy photons. The circuits we present are formed with Josephson junction arrays where strong quantum phase-slip fluctuations are present either in all of the junctions or in only a single junction. The quantum phase-slip fluctuations are shown to result in the strong inelastic photon-photon interaction observed in both circuits.

The phenomenon of a single photon decay provides a new way to study multiple long-standing many-body problems important for condensed matter physics. The examples of such problems, which we cover in this work include superconductor to insulator quantum phase transition in one dimension and a general quantum

impurity problem. The photon lifetime data can be treated as a rare example of a verified and useful quantum many-body simulation.

INTERACTING PHOTONS IN CIRCUIT QUANTUM ELECTRODYNAMICS : DECAY OF THE COLLECTIVE PHASE MODE IN ONE-DIMENSIONAL JOSEPHSON JUNCTION ARRAYS DUE TO QUANTUM PHASE-SLIP FLUCTUATIONS

by

Nicholas Christopher Grabon

Dissertation submitted to the Faculty of the Graduate School of the
University of Maryland, College Park in partial fulfillment
of the requirements for the degree of
Doctor of Philosophy
2020

Advisory Committee:
Professor Vladimir Manucharyan Chair/Advisor
Professor Jay Deep Sau
Professor Steven Anlage
Professor Victor Galitski
Professor Ichiro Takeuchi, Dean's Representative

Acknowledgments

"If I have seen further it is by standing on the shoulders of Giants.", -Newton. There is a famous paradox called "The ship of Theseus". It is supposed that the famous ship sailed by the hero Theseus in a great battle was kept in a harbor as a museum piece, and as the years went by some of the wooden parts began to rot and were replaced by new ones; then, after a century or so, every part had been replaced. The question then is if the "restored" ship is still the same object as the original. A modern extension notes that our bodies are continually being replaced by new cells taking over from the previous ones. Here we all agree that I am the same person as I was ten years ago even though I am now made of entirely new cells. My identity is found not in the physical things that make me up but rather the design or organization of those parts. What is preserved is my patterns of thought, memories, and opinions. However many of these patterns of thoughts or opinions are those of others taught to me throughout the years. The DNA code that determines my hair color or blood type is derived from my parents which is in turn was derived from there parents. My identity is therefore inextricably tied with all those who influenced me. The name, 'Nicholas Grabon', refers then not only to the particular physical body writing this but also all those other individuals connected to me. The experiment in chapter 4 is a great illustration of this. In analogy each

individual is like the impurity while the individual's community is the set of chain modes. For small coupling we can look at the impurity and the chain modes as being distinct entities. However as the coupling increases this distinction falls away. The resonances we measure are now inseparable combinations of the two. In this sense, the work done in thesis is as much attributable to everyone who supported me as it is to me. My deepest gratitude goes to my advisor Vladimir Manucharyan. I owe my progress as a scientist to him. He has supported and guided my progress in knowledge and way of thinking over these years I worked in his lab. When I joined the lab it was mostly empty and we built it from scratch. It has since grown past the walls into multiple labs. This is a great metaphor for my growth as a scientist. Vlad took so much time and persistence to make sure we understood what was going on at the deepest level. He challenged me constantly to improve the coherence of my thoughts and the quality of my work. Often I have been slow to learn, but he showed great patience with me throughout. In retrospect, this was the perfect place for me. I have very much enjoyed the subject matter and the research I had the privilege to do under his leadership. Thank you for being such a great advisor. My sincere thanks go to Prof. Steven Anlage for teaching me the fundamentals of superconductivity. The phenomenon of superconductivity is central to this work and your teaching has proven quite useful. Thank you to Prof. Jay Sau for teaching me the basics of topology in condensed matter physics. It was a real pleasure to from you. Also thank you for writing a paper helping understand our experiments on the homogeneous chains. Thank you to Prof. Victor Galitski and Prof. Ichiro Takeuchi for agreeing to read and review my thesis and sit on my committee. I know it is a lot

of work. I am very grateful also for our postdoc, Roman Kuzmin, who was always there to answer my questions and was patiently helping me whenever I struggled with anything. Our research has progressed so well in big part due to his dedicated efforts to set up and run the experiments properly. Thank you to all my colleagues in the lab, with whom we had many interesting and challenging conversations over the years. Special thanks to the poker crew for the many nights I was able to lose money to you. Last but not least, I would like to extend my gratitude to my family, who has supported and encouraged me throughout my journey. Thank you to Mom and Dad who did everything they could to help me succeed. Thank you for all the lessons and love you have given me. Thank you to my wife, Tjasa, who has patiently pulled overnighters, motivating me to push through the writing block and other struggles.

Table of Contents

List of Tables

List of Figures

List of Abbreviations

1D	One dimensional
AC	Alternating current
BKT	Berezinski–Kosterlitz–Thouless
BSG	Boundary sine-Gordon
C	Celsius
cQED	Circuit quantum electrodynamics
dBm	Power ratio in decibels (dB) of the measured power
DC	Direct current
GHz	Gigahertz, 10^9 Hz
HEMT	High-electron-mobility transistor
IPA	Isopropyl Alcohol
K	Kelvin
MMA	Methyl methacrylate
PMMA	Poly(methyl methacrylate)
SEM	Scanning electron microscope
SI	Superconductor-insulator
SQUID	Superconducting quantum interference device
VNA	Vector network analyzer

Chapter 1: Introduction

An array of Josephson junctions implements one of the simplest many-body models undergoing a superconductor-insulator (SI) quantum phase transition [1, 2]. Apart from zero resistance, the array's superconducting state is necessarily accompanied by a sound-like mode due to collective oscillations of the phase of the complex-valued order parameter [3, 4]. Exciting this collective phase mode results in transverse photons propagating along the array. Surprisingly little is known about the fate of this mode upon entering the insulating state, where the order parameter's amplitude remains non-zero, but the phase ordering is "melted" by quantum fluctuations [5].

The main goal of this thesis work is to explore the effect of quantum phase-slip fluctuations on the collective phase mode in Josephson junction arrays. Two limiting cases are studied. First, we start with homogeneous chains of Josephson junctions forming a telegraph transmission line where every junction is subject to the quantum phase-slips [6]. Second, we look at a system where the quantum phase-slips are localized to a single spot [7]. In both cases, the quantum phase-slips are shown to create strong interaction between transverse photons resulting in a single photon decay into multiple lower energy photons. Such an unusual behavior of single photons is reported for the first time. We believe that the observed photon decay

process plays an important role in the dynamics of superconductors in the vicinity of superconductor-insulator transitions.

In this chapter, we will introduce the Josephson junction transmission lines where the phase mode can be observed. Such lines, thanks to the large kinetic inductance of the Josephson junctions, implement a one-dimensional media with an effective fine structure constant of order unity. The later fact is crucial to achieve strong interaction effects observed in this thesis work. Then, we will describe a superconductor-insulator quantum phase transition which is expected in the Josephson junction arrays with large enough fine structure constant. Finally, we will provide a background for the research on the Josephson junction arrays with phase-slips localized to a single junction. Such systems can simulate a large number of strongly-correlated models known as quantum impurity problems.

1.1 Physics of Josephson junction transmission lines

A classical transmission line is often modelled as a sequence of inductors and capacitors as shown in (Fig. 1.1). Such line realizes a one-dimensional vacuum which hosts electromagnetic waves as current flows through the inductors and charge builds up on the capacitors. This vacuum can be characterized by an effective fine structure constant $\alpha = Z/R_Q$, related to the line's characteristic impedance $Z = \sqrt{l/c}$ and the resistance of quantum $R_Q = h/(2e)^2 \approx 6.5\text{k}\Omega$, which controls the fluctuation of electric field and defines the strength of light-matter coupling.

In order to explore the effects of large quantum fluctuations, we need the ef-

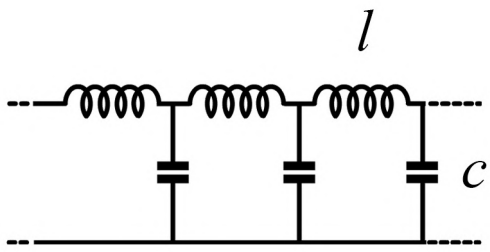

Figure 1.1: Simple transmission line circuit model. The inductance, l, for us will be provided by a Josephson junction. Both the inductance, l, and capacitance, c, are per unit length.

fective fine structure constant to be of order unity which translates to $Z > R_Q$. Creating a transmission line using only geometric inductors will result in an impedance that marginally differs from the impedance of vacuum 377Ω. The element that we can use that gives high inductance and low loss is a Josephson junction.

A Josephson junction is any sort of weak link between two superconductors. When the superconductor is broken up by the weak link, the phase of the order parameter can be different on either side of the junction. The result of solving the quantum mechanical tunnelling problem is that a supercurrent will develop if there is a phase difference ϕ across the junction, $I = I_C \sin\phi$ [8, 9]. The prefactor I_C is the critical current of the junction. The critical current depends on the specifics of how the junction was made and it is proportional to the area of the junction.

In general, a Josephson junction can be viewed as a non-linear inductance element. If the phase difference varies in time, a voltage will develop across the junction, $V = \frac{\Phi_0}{2\pi}\frac{d\phi}{dt}$. Here $\Phi_0 = \frac{h}{2e}$ is a fundamental scale known as the flux quantum. Note that if we identify a flux as $\Phi = \Phi_0\frac{\phi}{2\pi}$ we find this equation for voltage now becomes analogous to Faraday's law for magnetic fields $V = \frac{d\Phi}{dt}$. The

flux here is stored not in the magnetic field but in kinetic energy and thus the associated inductance is known as kinetic inductance.

Combining the equations for voltage and current we can find the energy stored in the junction, $E_{Junction} = \frac{I_C \Phi_0}{2\pi}(1 - \cos\phi)$. For small phase differences we can expand the cosine term. Now we get an energy that is analogous to inductive energy, $\cos\phi \approx 1 - \phi^2/2$ thus $E_{junction} = \frac{I_C \Phi_0}{2\pi}\phi^2/2$. We can then identify the inductance associated to this junction as $L_J = \frac{1}{2\pi}\Phi_0/I_C$, and take the prefactor as $E_J = \frac{I_C \Phi_0}{2\pi}$.

As we can see, at small enough phase differences a Josephson junction will act as an inductor. We can use it to make our Josephson junction transmission line (Fig. 1.2). This transmission line is constructed using two chains of Josephson junctions. Each chain has 16,000 junctions which leads to a length of 10 mm. These junctions act as the inductors of our transmission line with the characteristic energy scale E_J. The classical capacitance of the two metal chains next to each other gives the capacitance to ground and the corresponding energy scale E_0. We make the chains as compact as possible to reduce this capacitance and thus keep the impedance high. In fact, in this thesis work we will demonstrated the impedances up to 23 kΩ, which are equivalent to the effective fine structure constant exceeding one.

The chains are connected at one end to an antenna and connected together on the other giving an open and short boundary condition, respectively. The phase mode in this system corresponds to AC current through the junctions and AC electric field across the two chains. The spectrum of the phase mode excitations is discrete due to the finite length of the chain. Because of the boundary conditions, the lowest frequency mode corresponds to a quarter wavelength.

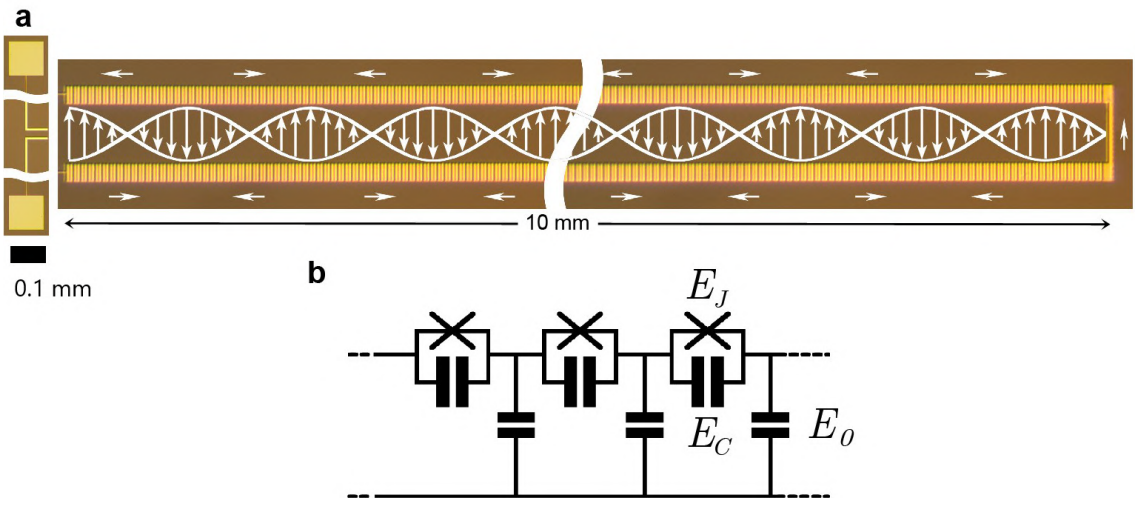

Figure 1.2: (a.) Optical photograph of the Josephson transmission line with a dipole antenna at the left end and a short-circuit termination at the right one. Arrows represent the AC current through the junctions and AC electric field across the two chains. (b.) Circuit diagram for the model of our transmission line. E_J is the energy associated with the Josephson junction. E_C is the energy associated with the capacitance of the junction. E_0 is the energy associated with the capacitance between the two chains.

In addition to the inductive term of the junction there is also a capacitance that arises from the classical effect of having two islands of metal a short distance away from each other. The energy associated to this is, $4E_C q^2$. Here $E_C = e^2/2C_J$ with C_J being the capacitance of the junction, with q being the charge on the capacitor in units of 2e. This energy combined with the inductive term defines the plasma frequency of a junction, $\omega_p = \sqrt{8E_J E_C}$. This frequency is independent of the junctions area and is a characteristic of the weak link. The diagram including all these terms is shown in (Fig. 1.2b).

The phase across the junction and the charge are both quantum variables. Moreover they are conjugate, $[q, \phi] = i$. Thus both cannot be fixed at the same time. The energy of the Josephson term is periodic with phase. Thus it has periodic

minima in which the phase could sit in equilibrium. Classically the only way to traverse between the minima is through the addition of thermal fluctuations that can supply enough energy. However quantum mechanics allows for a rare tunneling through the barrier. Such an event is called a quantum phase slip [10, 11]. As the phase slip rate increases the phase becomes less ordered. This destruction of phase order will lead to charge being ordered and thus an insulating state. Such a transition from a superconducting to an insulating state is an example of a quantum phase transition.

1.2 Current understanding of superconductor to insulator phase transition in Josephson junction chains

Quantum phase transitions are phase transitions driven by quantum fluctuations instead of thermal fluctuations. In the superconductor to insulator transition, quantum phase slips drive the system from having the phase ordered, a superconductor state, to having the charge ordered, an insulating state. Bradley and Doniach first predicted a superconductor to insulator quantum phase transition in Josephson junction chains [2]. They modeled it as a chain of junctions with a capacitive coupling to the ground. They found that this model can be mapped onto a two-dimensional XY model. This transition belongs to the celebrated Berezinski–Kosterlitz–Thouless (BKT) type and is driven by the competition between phase and Cooper pair number fluctuations [1, 12, 13]. Further studies that included both the capacitance to ground and the capacitance between islands predicted a transition

to the Mott insulator at $\alpha_c^{Mott} \approx 1/4$ [14] [15].

A more realistic model should include a random charge offset at every island. In this case, the chain realizes a disordered Tomonaga–Luttinger liquid with the fine structure constant α replacing the inverse Luttinger interaction parameter[16] [17] [18]. Theory then predicts a compressible insulating state, termed 'Bose glass', at $\alpha_c^{BG} = 1/3(Z = 2.2k\Omega)$ [19]. This state contains disconnected superconducting domains amidst a general insulating landscape. The insulating nature comes from the fact that the domains are of finite size and spatially separated such that tunnelling between them is suppressed.

Bard et al. [17], find the resistivity of Bose glass states close to the transition decreases until the temperature is 10^{-4} times the plasma frequency before eventually rising. For typical plasma frequencies of experiments, 20-25 GHz, this is well below 1 mK and thus well below the accessible temperature range of any experiment. Thus resistivity measurements at these temperatures cannot distinguish which state the chain is in. In addition, they find non-monotonic length dependence for devices with lengths less than 10,000 junctions. Thus DC measurements with current experimental setups cannot probe the quantum critical point.

Although the critical point is formulated in terms of the wave impedance of the collective mode, most of the previous experiments on the chains of Josephson junctions were in DC domain [18, 20, 21, 22, 23]. These experiments were limited to hundreds of junctions and temperature in the tens of mK. In the experiment by Chow et al. [20], they looked at chains of 255 SQUIDs and measured the resistance as a function of a temperature down to 20 mK, as a function of a magnetic field.

The magnetic field reduces effective E_J/E_C of a SQUID allowing them to change chain parameters in situ. Initially the resistance goes down with the temperature. As the magnetic field increases they see a sharp rise in resistance at the lowest temperatures. They associate this sharp rise in resistance with the effect of the insulating state. In the experiment by Haviland et al. [21] they also measured arrays of SQUIDs with many different parameters at 50mK. They found that the chains with SQUIDs having initial $25 > E_J/E_C > 6$ they can tune between high resistance and no resistance by changing the magnetic field. However, in devices with $E_J/E_C < 6$ they only find high resistance. In the experiment by Ergul et al. [22] they used chains of SQUIDs while they consider chains with particular weak link in the middle. They find the zero bias resistance of the uniform chains to have a kink at around $E_J/E_C = 16$. They also find similar behavior between chains with length 384 and chains of length 2,888. For the device with a weak link they find that this weak link dominates the resistance over the chain. From these studies it is clear that a transition occurs at some point but what is the control parameter and where exactly is the critical point were left unanswered.

Cedergren et al. considered DC resistance measurements of chains of Josephson junctions [18]. The chains varied in length from 250 to 5,000 junctions. They measured the critical voltage of these chains and the voltage's dependence on the phase slip rate of the junctions. They found the voltage increased alongside the phase slip rate with a particular scaling. They compared the scaling to the model given by the quantum theory of one-dimensional disordered bosonic insulators and found broad agreement. They also found that they need to include quantum fluc-

tuations to account for the data, so classical depinning theory is not enough.

Most of the previous experiments on the superconductor–insulator transition (SIT) focused on finding a universal scaling of (zero-frequency) DC resistance with temperature and other system parameters [24]. The quantum BKT transition resisted such an approach, possibly due to a combination of the system's finite size, poor knowledge of actual temperature and microscopic parameters, or lack of equilibrium under a DC bias. In fact, disorder can make the resistance scaling on temperature non-universal [17]. In the chapter 3 of this thesis work, we avoid these issues by asking a conceptually different question: how is the propagation of the phase mode, at frequencies higher than temperature, wavelengths much shorter than the system size, and excited with less than a single photon, being inhibited in progressively higher impedance chains? $\varphi(x)$

1.3 Quantum phase slips

Quantum phase slips have been predicted to induce inelastic scattering of the phase mode [25, 26]. Here the quantum phase slips cause a single probe photon to decay into a large number of lower-frequency photons. However, this is not the only way in which decoherence could arise in our system. Decoherence is also predicted to arise from the pinning of a charge density wave, which is a dual representation of the phase mode [27]. This causes an inhomogeneous broadening of the standing wave resonances after ensemble-averaging of their frequencies over disorder. This can indeed occur in a single device due to fluctuation of the offset charges in time.

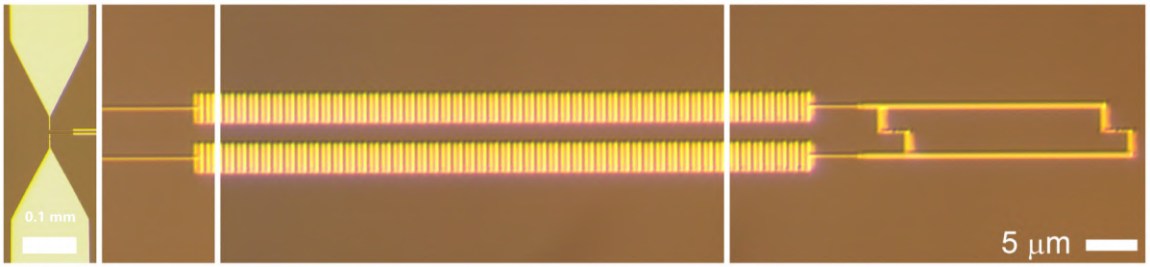

Figure 1.3: Optical photograph of a Josephson transmission line with a single phase-slip junction connected to the line's end. The antenna is on the left, the transmission line is in the middle, and the SQUID is on the right.

To better understand the effect of the quantum phase-slips on the collective phase mode a simpler system could be used. Instead of having every junction in the array subjected to large quantum fluctuations, we can study how the phase mode in a superconducting Josephson transmission line is affected by a single phase-slip junction connected to the line's end. Using such a system (Fig. 1.3), in chapter 4 we will show that a single photon can inelastically scatter on a quantum phase slip.

Inelastic scattering of photons on a phase-slip junction can also be related to the physics of various quantum impurity models, which opens the way to analog quantum simulations. Goldstein et al. described an example of inelastic scattering by considering the effect of an interruption of a chain of junctions by an 'impurity', which is a capacitance and two weaker junctions [28]. They find that they can map this problem to a spin-boson model with Ohmic dissipation which is equivalent to the single-channel Kondo model [29, 30]. They then relate the transmission coefficients for scattering off the impurity to the local dynamic differential spin susceptibility of the Kondo problem. By measuring this transmission coefficients, we could get

the hard to access dynamic susceptibility of the Kondo model. While simulation of the Kondo model in particular, achievable by shunting the impurity junction with an impedance, is left as a future extension of this work, it is nevertheless helpful to understand the systems presented here.

The difficulty of the Kondo problem lies in the fact that the coupling strength between the impurity and the bath continues to grow and would seem to diverge as the temperature goes to zero. Thus, calculating the reflection coefficient for scattering off this impurity is quite challenging. Instead we can find the coefficient by doing an analog quantum simulation of this model. Such simulation works by making a physical quantum system that has the same physics as the problem under consideration. By experimentally measuring specific quantities of this system we can use nature's "solution" in the form of dictating how the system responds as our method of solving the problem. The experiments presented in this thesis can be treated as analog quantum simulations of the superconductor insulator transition and a particular quantum impurity problem.

Chapter 2: Experimental Methods

2.1 Fabrication procedures

There are many ways to make a Josephson junction. The junctions we use are aluminium-aluminium oxide-aluminium tunnel junctions. These are sandwiches of aluminum with the interior being a thin layer of aluminum oxide. Here the weak link is the insulating layer of aluminum oxide. We choose this because the aluminum oxide that grows is unique in that it is self-terminating and thus has reliable thickness for the junction. This is important as the critical current and thus E_J is exponentially sensitive to this width. In addition there has been much study in use of these junction and methods have been found to grow low loss junctions [31].

The procedure we use to make these junctions is known as the Dolan bridge technique [32]. The majority of our procedures follows from the procedure established by Frunzio et al. [33]. We use silicon wafers with high resistivity, greater than 10 kOhm*cm. For the mask, we use MMA, Methyl methacrylate, and PMMA, Poly(methyl methacrylate), double layered resist aiming at 500 nm of thickness for MMA and 100 nm for PMMA. The mask is patterned using a Elionix electron beam lithography system. It has the capability to stitch together write fields over a large

range of distance, ≈ 10 mm, with little if any stitching errors. This is important as the chains we make are often this length, but the write field is much smaller. It also has a laser that can determine the height of the surface and then it can adjust the focus accordingly. This allows the beam to still be in focus as travels over height changes in the surface. When it is not in focus the beam bleeds into the bridges and the bridges collapse which destroys the usefulness of the pattern.

After writing the pattern is developed in a mixture of three parts IPA, Isopropyl Alcohol, to one part water. The mixture is kept at 6 C in a cooling bath.

The deposition of aluminum is performed in a Plassys e-beam evaporation system, where we start with a descum step that will remove any remaining organics from the surface. We do this twice at each angle we will later deposit the aluminum at. Then we deposit 20 nm of aluminum at a steady 1 nm/sec. Then we do a static oxidation step for twenty minutes at 100 mBar. We tested a number of different pressures and found this value to give more consistent junction parameters. After this step we do another aluminum deposition at the other angle but now for 40 nm thick. Finally we do a final oxidation at 10 mBar to give a capping layer for the device which ensures a consistent top interface. The examples of a junctions array and of a single small junction made in this process are shown in Figure 2.1.

We make our devices in a piece wise manner rather than on whole wafers. We do this because we need to make many different devices each with designs that can only be known after measuring the previous device. We start by cleaving the wafer. To do this we first take a diamond scribe and make a small scratch at the edge of the wafer. We do this at the distance desired measured with a caliper. Then holding

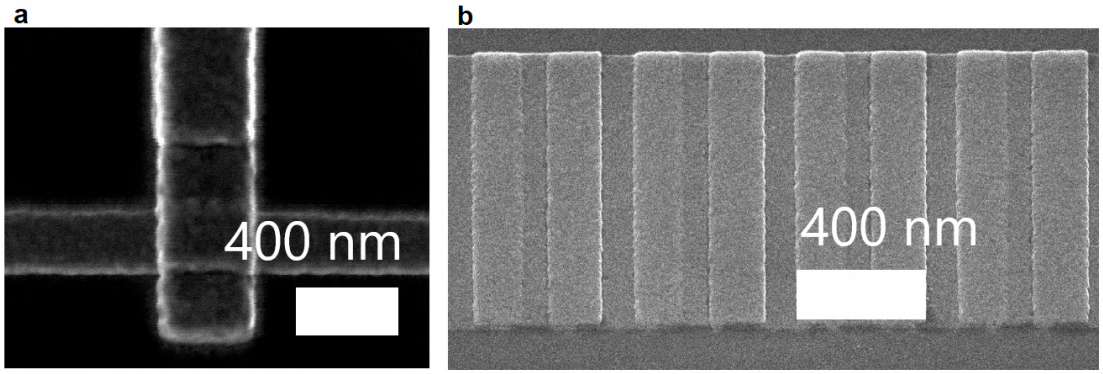

Figure 2.1: a.) An example of a typical impurity junction. b.) An example of a section of a chain of Josephson junctions. Each rectangular piece of metal corresponds to an island. The junctions are formed at the overlap between the islands. The oxide cannot be seen in this photograph.

the wafer in one hand with a forceps we gently squeeze along the scratch with a cleaving pliers. This pliers will hold and gently crack the wafer along the scratch. Pressing too hard will result in the wafer shattering, so it takes some practice with dummy wafers to get the hang of it. This first cut will result in a long section of wafer we will then cleave even further into our desired dimension. One general important principle is to treat any part of the surface that is touched by something else as forever unclean.

2.2 Reproducibility of junction plasma frequency

In order to characterized the junctions' parameters and check their reproducibility, we employed two approaches. The first approach is based on the measurement of waves' dispersion in fabricated Josephson transmission lines as will be discussed in chapter 3. This approach provides a very accurate measure of an averaged junction's plasma frequency, and, therefore, allow us to qualify junction's

oxide.

A simpler way to characterized a Josephson junction is by measuring its room temperature resistance. In this approach, we use chains of junctions or single junctions attached to large pads of aluminum. We can then touch these pads with metallic needles which allows us to find the resistance of the chain or junction. There is a well known and often used formula that relates the resistance of a junction at room temperature to its critical current when superconducting [34]. This theory is for a single junction but we have found that chains with ten to a hundred junctions scale linearly with junction number. Furthermore when we cool down the chains we find that the parameters we infer from the spectrum match what we measure with resistances.

To test homogeneity of junction's parameters along the array, we placed pads at regular intervals throughout the chain and measured the resistance between segments. We found that the chains had similar resistance as their neighbors but over the course of the whole chain there was significant drift. This suggests that long range disorder is the dominant type of disorder. In addition when measuring the areas of the chain junctions we found that there was very little if any difference in area from the beginning to the end separated by six millimeters or more. Thus we conclude that it is the oxide itself that is causing these inhomogeneities.

As a result of our tests, we found the chip to chip variation in the measured resistance to be around 10 percent and the within chip variations of around 2-3 percent, which is common among other labs [35, 36, 38]. We ran a number of tests to try to find what might be the important limiting factor for more precision. Hu-

midity is one possible culprit. We have measured the humidity in our lab to be a fairly consistent 40 percent due to the climate control installed. However, we have noticed that the humidity changes in the fall when the air conditioning is turned off and heating is turned on. We have seen some rough correlation with the measured plasma frequencies.

Our deposition machine is automated so that a computer controls basically all steps. This helps ensure uniformity and removes the operator as a source of variance. We found that how long one pumps on the sample before deposition has a significant effect on the resulting resistance. Moreover pumping for shorter periods of time seems to be correlated with higher variability. We settled on pumping overnight for all our devices.

When junctions are exposed to ambient conditions, room temperature and pressure while exposed to air, they tend to change properties over time or 'age'. Thus when the sample is measured, this needs to be taken into account when assessing precision. How they age is dependent on the details of the fabrication setup. A leading theory is that elements other than oxygen are absorbed into the oxide[37]. We found that the resistance of our junctions increase over time in consistent manner. The growth follows a trend similar to exponential decay with time constant of two to three days. However it did not fit to any exponential fit we tried. Moreover when we collected the plasma frequencies obtained from fitting the dispersion we found a similar pattern. (Fig. 2.2). This dependable growth can be used as a tool to change the parameters of a device. By simply removing the device from vacuum into ambient condition will cause the inductance and therefore impedance of the

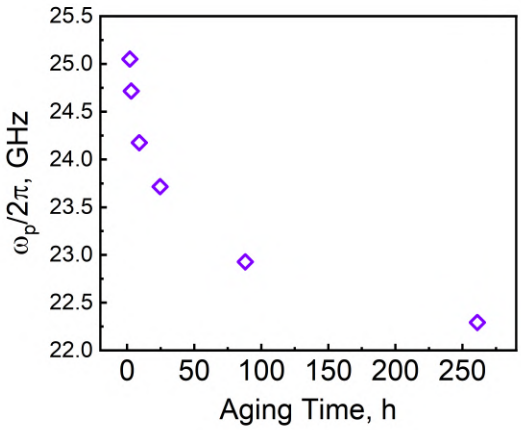

Figure 2.2: The measured plasma frequency of our chains as a function of time. Each point represents the same waveguide measured after aging the listed amount of time. The plasma frequency is obtained by fitting the dispersion with a known formula, (Fig. 3.4).

transmission line to grow. We can then keep the junction area and capacitance exactly the same but in a device with a different impedance. Thus we can isolate the effect of impedance from junction area which is especially critical since the SIT exponentially sensitive to junction area.

2.3 Sample loading

Assuming everything went well we then load the sample into a copper waveguide. The chip is aligned so that the antenna is parallel to the electric field in the waveguide. This waveguide is a box designed to pass frequencies in the range at which we measure. The box has dimensions of 9mm x 27 mm x 25mm. It has one port connected to a microwave launcher and the other port is grounded. We perform a one port reflection measurement. It has a small shelf which the chip sits on as can be seen here (Fig. 2.3). We make sure the chip stays in place by placing

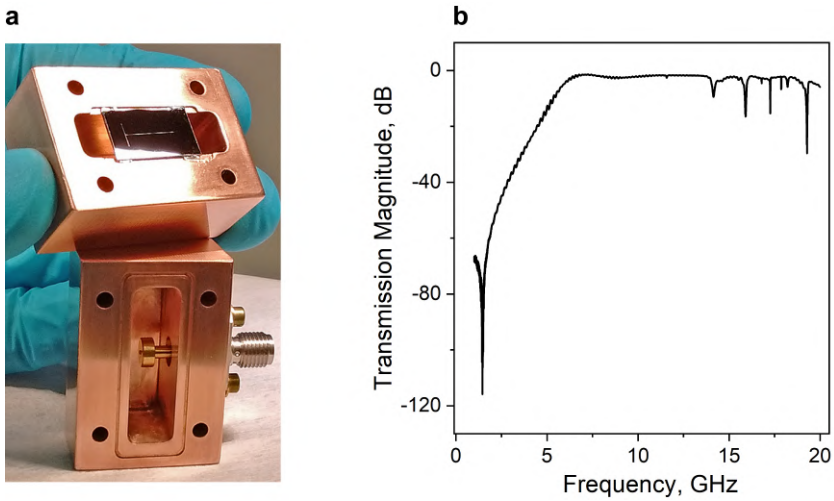

Figure 2.3: a. An image of the sample mounted in one of the copper waveguides. The extended antenna in the bottom half is what allows for transmission over a broad range of frequencies. b. The transmission of the copper waveguide at room temperature.

four small dots of indium under the corners of the device. Too much more can lead to problems removing the device. We then close the box and screw it onto a cold finger of our dilution refrigerator.

2.4 Microwave setup

The dilution refrigerator a majority of our devices were tested in has a fast swap mechanism. It has a probe that can be inserted or removed while the rest of the fridge stays cold and under vacuum. Because the probe's volume is small it can be cold fast. We have often removed a device inserted the new device and the new device ready to measure the next day. This has been instrumental in allowing us to measure many different samples.

Inside the dilution refrigerator we have microwave lines that connect to and

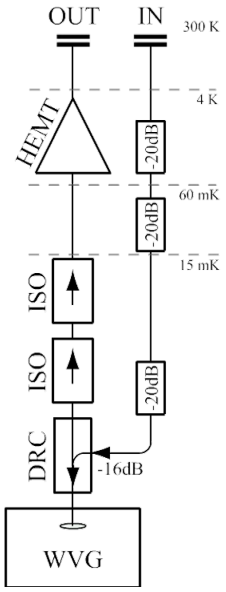

Figure 2.4: The setup of the microwave lines used in all measurements. HEMT - high electron mobility cryogenic amplifier, ISO - cryogenic broadband isolator, DRC - directional coupler, WVG- copper waveguide holding the sample.

from the sample (Fig. 2.4). Going to the sample we have three 20 dB attenuators placed at different stages of the refrigerator. These attenuators serve to reduce the power of the incoming signal and clean out thermal noise. Since the noise generated at a particular point depends on the point's temperature we want to have the attenuators at as cold of temperature as we can get. However, our refrigerator has a finite amount of cooling power with more cooling power at hotter stages. Thus there is a balance needed to reduce the noise as much as possible without heating up the stages. Our solution was to place one attenuator at the 4K, the 60 mK, and the 15 mK stages. After these attenuators is a directional coupler that then connects to the waveguide.

Going away from the sample are two isolators to prevent back action. Then there is a HEMT amplifier at 4 K and then a room temperature amplifier outside

the dilution refrigerator. These amplifiers are necessary to get a signal with power that we can measure. In addition there are DC lines, not shown in figure, used to generate a magnetic field. The magnetic field was generated using superconducting wire that was wrapped around a solenoid near the sample to create an uniform field.

We took the vast majority of the data presented with a four port vector network analyzer, VNA. This device sends out a microwave tone at a specific frequency and power. It measures the reflected signals amplitude and phase. The ratio between the input and output gives the reflection coefficient used to find the resonance modes and their quality factors. We controlled the VNA and the magnetic field with Labview.

Chapter 3: Microwave spectroscopy of homogeneous Josephson junction chains

In close analogy with vacuum quantum electrodynamics, zero-point fluctuations of fields in our 1D Josephson junction arrays are controlled by the effective fine structure constant $\alpha = Z/R_Q$, where $R_Q = h/(2e)^2 \approx 6.5k\Omega$ is the resistance quantum for Cooper pairs [39]. The superconducting state is favoured for $\alpha \ll 1$, when the line mimics the usual weak-coupling electrodynamics of the free space, for which $\alpha = 1/137.0$. This is not a coincidence: at a given frequency, the Josephson relation links the fluctuation of phases across the junctions with the fluctuation of electric field between the chains, which in turn defines the strength of light–matter coupling.

Driven by quantum phase-slip fluctuations, the lines transition to an insulating 'Bose glass' state, which is predicted to happen at $\alpha_c^{BG} = 1/3(Z = 2.2k\Omega)$ [19]. In this chapter we explore how the phase mode excitations are being affected in the chains with progressively higher α.

3.1 Device layout

A typical device we use in this experiment is composed of two long chains of Josephson junctions shorted on one end and connected to an antenna on the other (Fig. 1.2a). The chains are 10 mm long or 33,000 junctions. The minimal circuit model which describes our system comprise three energy scales (Fig. 1.2b). The junctions are described using the Josephson relations and associated energy scale E_J. The E_J is given by the critical current which is proportional to the area of the junction. Each junction, being two islands of metal close to each other, has its own self capacitance as well. The energy scale associated with this term is given by $E_C = e^2/2C_J$ and is inversely proportional to the area of the junction. Between each chain is a geometric capacitance, C_0, with associated energy scale $E_0 = e^2/2C_0$. Given all these terms the resulting device hosts standing wave modes which we explore with the help of microwave spectroscopy.

3.2 Data

3.2.1 Two-tone spectroscopy

Our microwave setup allows us to get a good one tone signal from 4 to 12 GHz. However, the isolators in our system cut signals below 4 GHz. Thus to find the frequencies of the lower modes we use a different technique. The experiment is performed using standard two-tone dispersive reflectometry, taking advantage of the weak Kerr nonlinearity of a Josephson junction [40]. Here we utilize the fact

that all of our modes have interactions with each other. So when we shine power on one mode it shifts the frequency of other modes.

To obtain the two-tone spectrum, we continuously measure the reflection signal at a fixed read-out frequency within our microwave setup bandwidth while sweeping the frequency of a second tone. For the read-out, we usually choose the left shoulder of the resonance (Fig. 3.1a). The effect of shining the second tone is to reduce the center frequency of the other modes. It will shift the mode so that we measure the dip of the mode instead of the shoulder. This shows up as a dip in the reflection read-out signal.

Thus in scanning the pump tone we will find a set of dips in the read-out tone's reflection. These dips correspond to the other modes of our system (Fig. 3.2). Since we can shine in the pump tone without a problem, remember it was the isolators on thew way out that were the problem, we can access all the modes of our system down to the very first one. In accessing the first mode and then every consecutive mode we can be sure of the wave number for each mode. Because the shift in the mode is very dependent on the mode couplings and where we place the probe tone the depth of these dips is irrelevant for us.

3.2.2 Identification of the dispersion relation

The two tone measurements we have done have enabled us to find every mode of our system up to above 10 GHz and also know the wave number of these modes $k_n = \pi(n+1/2)/L$, where $n = 1, 2, ...$ and L is the length of the line. By indexing the

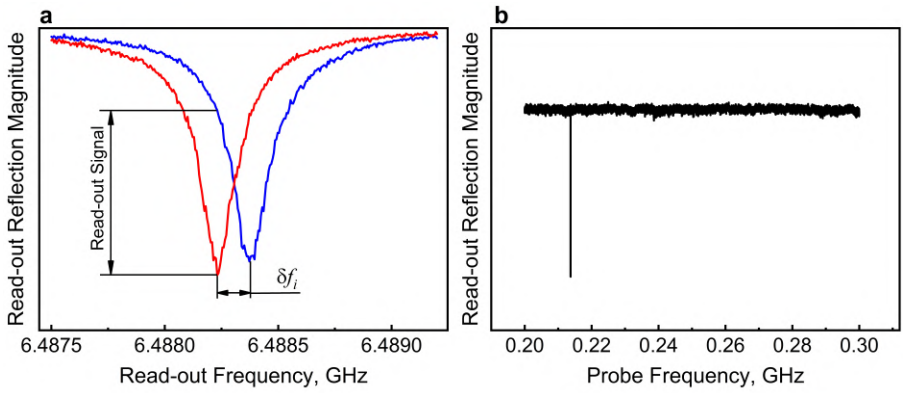

Figure 3.1: (a) The read-out mode while the probe tone is in (red) and out off resonance (blue) with the collective mode at 0.215 GHz. (b) The read-out tone reflection magnitude measured at the left shoulder of read-out mode line as a function of the probe tone frequency.

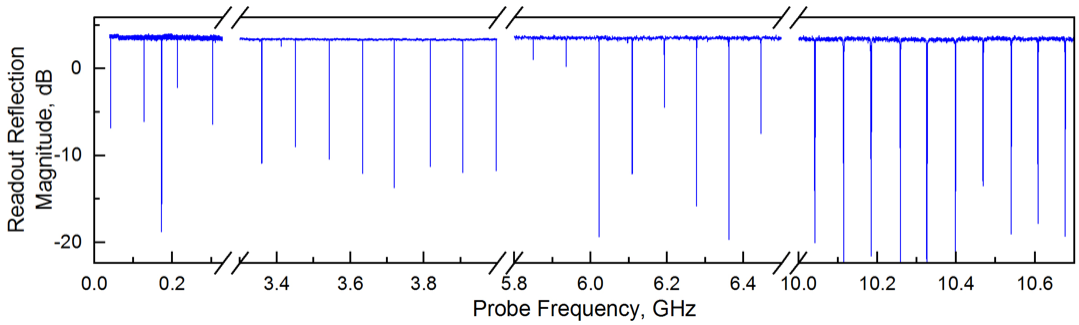

Figure 3.2: Reflection signal as a function of probe frequency. Discrete standing wave resonances are indexed one by one starting from the very first mode at about 40 MHz. The third resonance is a spurious mode and is discarded.

individual resonances and plotting the frequency as a function of the wave number, we obtain the dispersion relation $\omega_n(k_n)$, (Fig. 3.3). The dispersion is in excellent agreement with a simple two parameter expression $\omega(k) = vk/\sqrt{1+(vk/\omega_p)^2}$, describing photons with a velocity v in a telegraph-like transmission line with extra capacitance parallel to the junctions' inductance, which results in a band edge at the plasma frequency ω_p (Fig. 3.3).

The fit provides accurate values of v and ω_p, defined as $v = 2a\sqrt{E_J E_0}/\hbar$ and

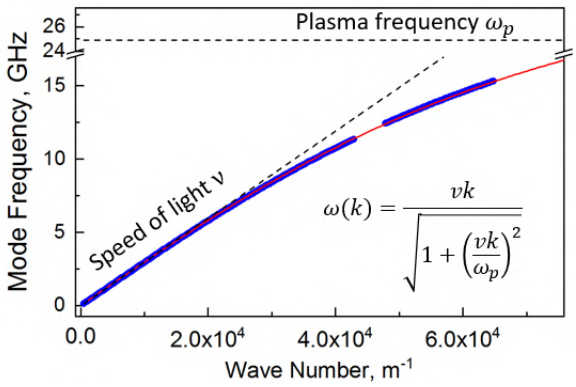

Figure 3.3: Reconstructed dispersion relation (blue markers) and theoretical fit (solid line).

$\hbar\omega_p = \sqrt{8E_J E_C} - E_C$. To find all three characteristic energy scales and as a result the wave impedance $Z = 2/\pi R_Q \sqrt{E_0/E_J}$, there is one more parameter that we need to estimate. We chose two ways to do it and compared the results. First we used the junction capacitance as the parameter. The capacitance of a aluminum oxide junction has been well characterized and known to just depend on the area of the junctions. We can then find the area of the junction by imaging it with a SEM. Alternatively we used the capacitance between the two lines. This value does not depend on the oxide and as the structures are quite large relative to the disorder in fabrication relatively immune to disorder. Here we use a known formula for the capacitance between two infinitely long coplanar strips [41]. The resulting values of the wave impedance differ by less than 20 percent which is the uncertainty of our estimation. The complete list of the parameters for the devices of chapter 3 is reported in Table 3.1.

3.2.3 Common modes

The fact that our transmission line contains two parallel chains of Josephson junctions results in two types of modes which the line can actually host. The first are differential modes which are the modes we measure in the rest of the experiments. The second are common modes. The differential modes have a voltage gradient across the two chains whereas the common modes have a voltage gradient from the chains to some ground (Fig. 3.4a). The ground for our system is complicated and hard to describe but since the device is separated by a large distance from the nearest metallic structure, the walls of the copper waveguide, this capacitance is much smaller than capacitance between the chains. The later fact can be checked by measuring the mode spacing for the common modes which can be excited at the lowest frequencies (Fig. 3.4b). Large spacings of the common modes indicate that the stray capacitances of individual islands to a ground are much smaller than the capacitance of the junction, so the theory for a single chain can be safely applied to our double-chain system [25, 42].

3.3 Signatures of the insulating state

3.3.1 Quality factors of standing wave resonances

To reveal the insulating state we measured the quality factors of the collective mode resonances. All the data were taken while populating the modes with much less than one quanta on average, and we checked that the spectroscopic line-shapes

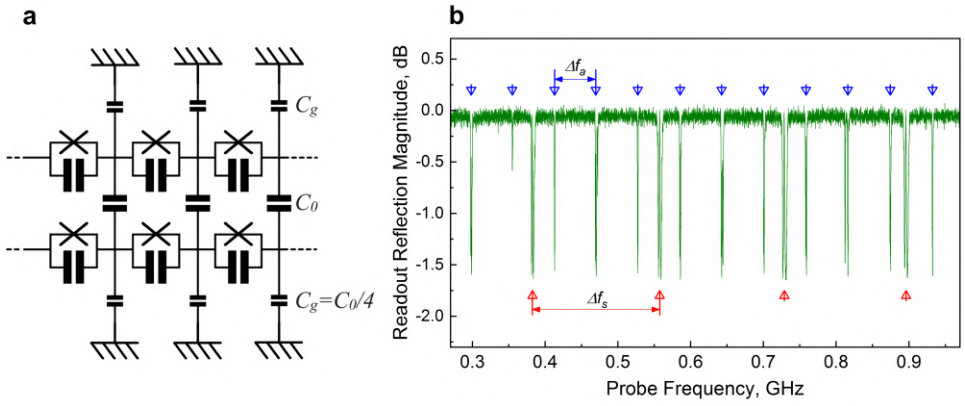

Figure 3.4: (a) Circuit model of a double-chain device with every island capacitively connected to ground. (b) Two-tone spectroscopy of the device d. Blue markers indicate differential modes and red indicate the common ones. The distance between adjacent arrows is the mode spacing for that type of mode. Δf_a is the spacing of the differential modes while Δf_S is the spacing of the common modes. The small splitting noticeable for some of the modes is an artifact of the large probe power required to see both types of the modes simultaneously

remained power-independent. A total quality factor Q_{tot} comprises two parts $Q_{tot}^{-1} = Q_{ext}^{-1} + Q_{int}^{-1}$. The first, the external quality factor Q_{ext}, measures how the system is coupled to its environment. The second, the internal quality factor Q_{int}, measure the losses within the system. The measured reflection coefficient, $S_{11}(\omega)$, is related to these quality factors in the following manner [43].

$$S_{11}(\omega) = \frac{2i(\omega - \omega_o)/\omega_o - Q_{ext}^{-1} + Q_{int}^{-1}}{2i(\omega - \omega_o)/\omega_o + Q_{ext}^{-1} + Q_{int}^{-1}} \tag{3.1}$$

We then take the data for a particular resonance around its resonant frequency ω_o and fit it with the previous equation to find the quality factors of that resonance (Fig. 3.5).

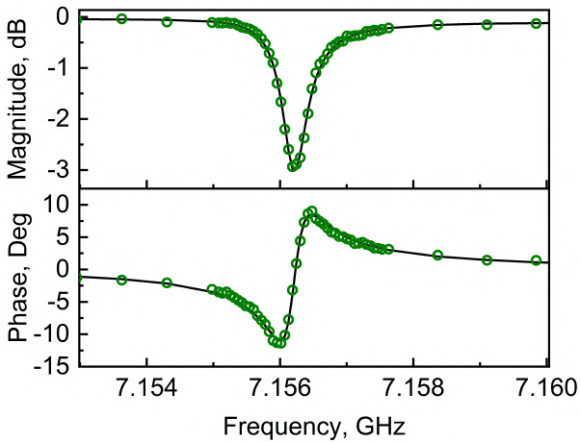

Figure 3.5: A typical example of the reflection coefficient magnitude and phase for one of the collective modes. The data (green circles) is fitted to a model 3.1 of dissipative LC-oscillator (black line).

3.3.2 Background dielectric loss

Our chains are subject to ordinary losses besides phase slips. In order to find the effect of phase slips we need to find which loss mechanisms impact our devices and calibrate them out. The main mechanism for our chains is due to dielectric loss. We can model this loss the following way,

$$Q_{int}(\omega) = \frac{2}{\tan\delta}\left(\frac{\omega_p}{\omega}\right)^2\left(1-\left(\frac{\omega}{\omega_p}\right)^2\right), \tag{3.2}$$

where $\tan\delta$ is the dielectric loss tangent. This model assumes the loss is in the dielectric of each junction as a shunting resistance. The value of this resistance is given by the loss tangent. We can then match this to our data (Fig. 3.6) to find the $\tan\delta$. This value is found to be consistent across all of our devices at around $\tan\delta = 10^{-3}$. A previous experiments has found a value similar to ours which they explained in terms of two level systems [44]. The data in (Fig. 3.6) corresponds to

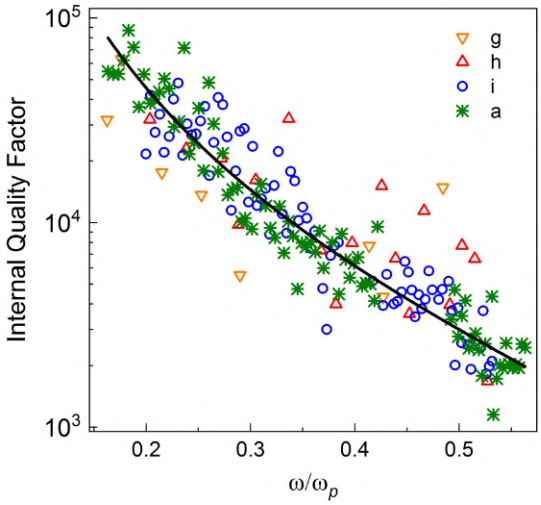

Figure 3.6: Internal quality factor as a function of the mode frequency normalized to the plasma frequency measured for several low-impedance Josephson transmission lines. The solid black line is the prediction for the internal quality factor limited by dielectric loss in the junction's oxide (Eq. 3.2).

the quality factors taken at one point in time. Repeated measurements of the quality factor were done to assess the stability of these values. The spread in obtained values is around two to three times the base value. Hence the variation from one frequency to the next cannot be distinguished from the variation in time of a single resonance. Potentially this could be due to fluctuating two level systems, but the data taken does not allows for any additional information about this variation.

3.3.3 Decay of the collective mode due to phase slips

We then investigated what happens when you reduce the transmission line's junction size which results in higher wave impedance Z and lower E_J/E_C. We kept the length and the distance between the chains the same. We saw little effect for junctions sizes greater than 0.4 um x 0.5 um, or $E_J/E_C \approx 90$ (Fig. 3.7). As we further reduced the junction area we noticed a change. The internal quality

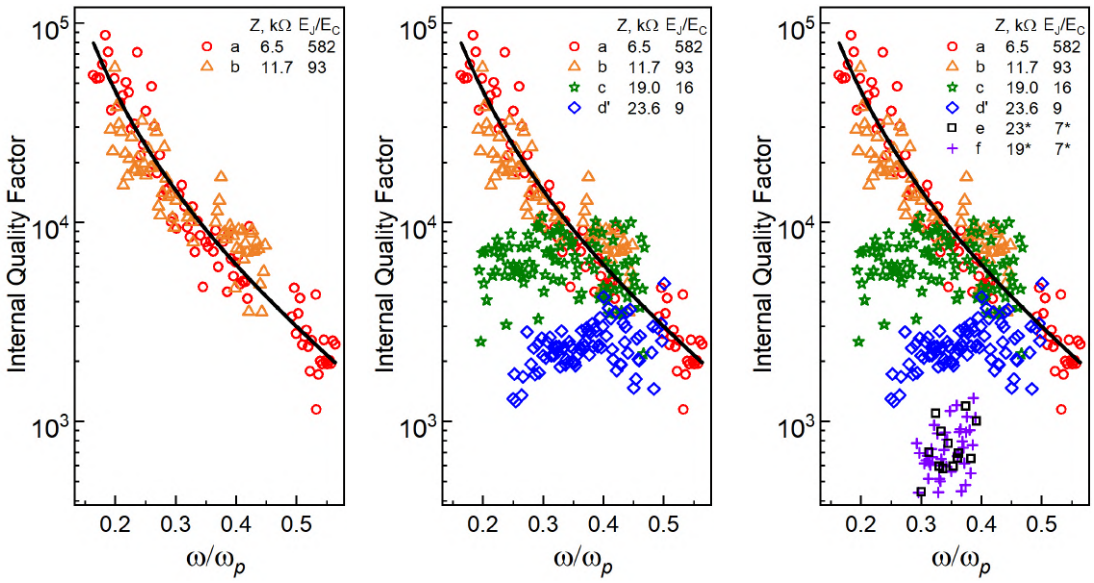

Figure 3.7: Extracted Q-factor plotted as a function of the mode frequency normalized to the plasma frequency. The black line is the fit to the background dependence due to dielectric loss.

factors at lower frequencies began to drop. Eventually the trend with frequency was reversed so that it increased instead of decreasing with frequency. This new loss mechanism could not be accounted for by dielectric loss. Furthermore the quality factor has dropped by over two orders of magnitude for some frequencies. In addition we found that it is E_J/E_C that controls this transition in quality factor behaviour rather than Z. We see this as device d', with impedance of 23.6 kΩ, has significantly higher internal quality factors, $\approx 2-3$x, than device f which has an impedance of 19 kΩ. However, device f does have a lower E_J/E_C than device d'.

3.3.4 Additional fluctuations in mode spacing beyond fabrication disorder

The modes of our device do not lie exactly on a dispersion curve but have some scatter in their frequency values. This disorder could come from a couple different sources. We found that when we remeasured a sample after aging the frequency fluctuations followed a similar pattern (Fig. 3.8). Images of the junction areas showed fluctuations in area too small to account for the fluctuations in mode frequency. The resistance test measurements, however, showed enough variation to account for the modes' frequencies fluctuations. Since the resistance is a combination of the effect of the oxide and junction area and the areas were found to not have enough variation that leaves the oxide as the source of the disorder. However, for the thinnest chains with the smallest values of E_J/E_C the disorder began to grow and exceeded what could be accounted for by the resistance tests indicating a new source of disorder. The mode spacings deviate in a Gaussian fashion. We define a quantity, δ, as the standard deviation of the measured distribution for each device. These quantities are the triangles plotted in (Fig. 3.10a).

3.4 Reversible transition from superconducting to insulating behaviour

We used the effects of aging and heating to show the change of quality factors in a single device. First we measured a device with $E_J/E_C = 11.3$ such that it was mostly dielectric loss limited (Fig. 3.9). Then we aged this device for 1,000

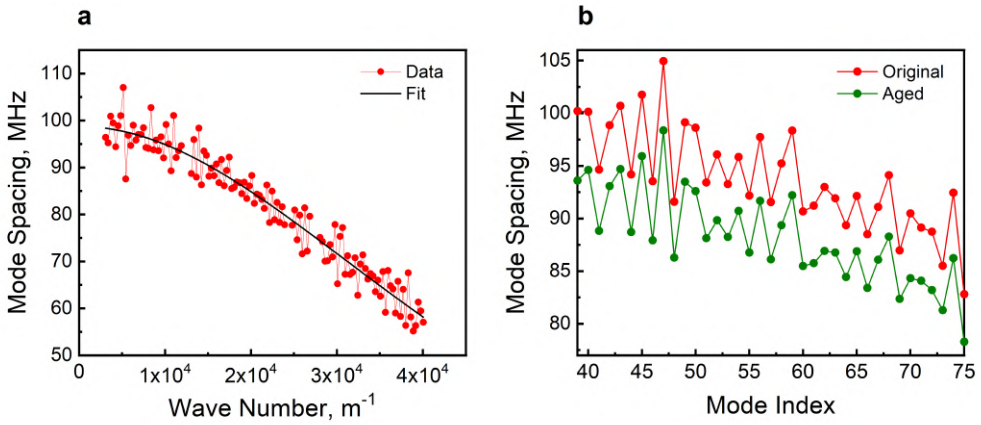

Figure 3.8: a. Mode spacing as a function of mode index. The sharp periodic outliers originate from the stitching error of the lithographer, otherwise invisible in device images. b. The frequency distance between adjacent modes as a function of the mode number. The green traces is the data from the same device as in red only warmed up to room temperature, left in ambient conditions for several days, and then cooled down again.

hours. This had the effect of increasing the inductance of the junctions and thus decreasing E_J/E_C to 8.7. When we measured this device the losses due to phase slips appeared, as expected for a device with this E_J/E_C. We then heated the device at 170 C for two hours as described in the Appendix A.1. When we measured this device we found that its E_J/E_C had risen back 10.6, as expected from the resistance test measurements. The device was now dielectric loss limited as it was at the start. The high sensitivity of the Q-factor to E_J/E_C (Fig. 3.7) and E_J (Fig. 3.9) unambiguously links the observed decoherence to quantum phase slips [11, 45].

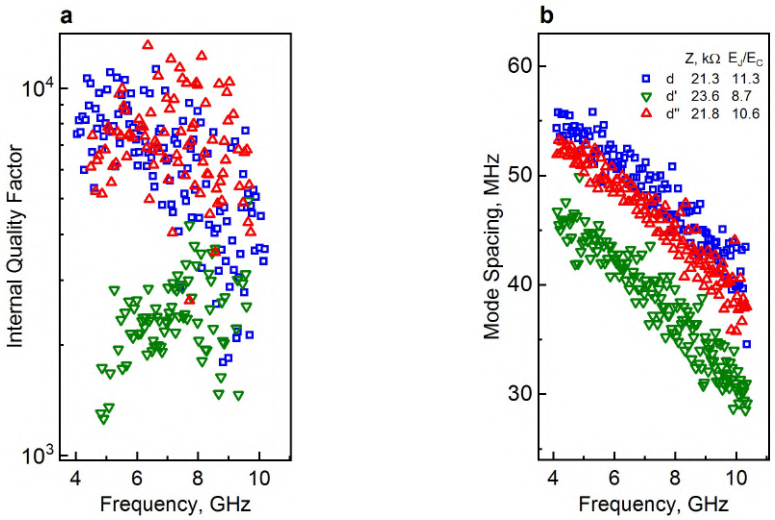

Figure 3.9: The Q-factor (a) and the mode spacings (b) as a function of frequency for the three subsequent incarnations of a single device: fresh after fabrication (blue), aged (green), and annealed (red). At 5 GHz the quality factor undergoes a remarkable swing by nearly an order of magnitude.

3.5 Characterization of the transition using pinning length and frequency

In the non disordered case for the SIT the system transitions into a Mott insulator. Here the charge is ordered as a charge density wave, (CDW). When disorder is present there will be sites that have larger capacitive energies that would be energetically favorable for the CDW to have the maximum voltage at. The charge then pins to these sites. As the disorder is randomly spaced the distance to the next pinning site will be incommensurate with the wavelength of the CDW. If the wavelength of a CDW is incommensurate with the lattice spacing, its energy will be independent of its phase [46]. Phase ordering can then persist in a limited fashion. There is a competition between the energy gained by pinning at a particular site versus the energy from the stiffness of the wave. This competition determines

the average length between pinning sites which in turn determines the length which phase can be correlated. The correlation length of the system is defined as the length, ξ, over which the phase at one site remains correlated with the phases less than that distance, ξ, away. Modes with wavelength shorter than this length can persevere since the phase can be correlated for shorter than this length. For our system, the correlation (pinning) length is found using the known device parameters as $\xi \approx (4E_0/W)^{2/\left(3-R_Q/Z\right)}$, where $W = 16/\sqrt{\pi}(8E_J^3E_C)^{1/4}\exp\left(-\sqrt{8E_J/E_C}\right)$ [46, 47]. The pinning frequency is the frequency of a mode with wavelength equal to the correlation length, ν/ξ. As the correlation length begins to approach the wavelength of the mode measured we find the fluctuations in modes frequencies grows rapidly (Fig. 3.10a). In any insulator correlated fluctuations will persist up to some finite distance. Normally this distance is so small compared to the other length scales that we can safely ignore this effect. The difference in our system is that we have a correlation length that is of a similar order as the mean distance traversed by a collective mode photon $Q\lambda_{probe}$ of wavelength λ_{probe}. Similarly as the pinning frequency begins to approach the probe frequency the decoherence rises. The modes with frequency larger than the pinning frequency have wavelengths shorter than the correlation length. The phase ordering of these modes is unstable. The instability reveals itself in our measurements as an additional source of decoherence.

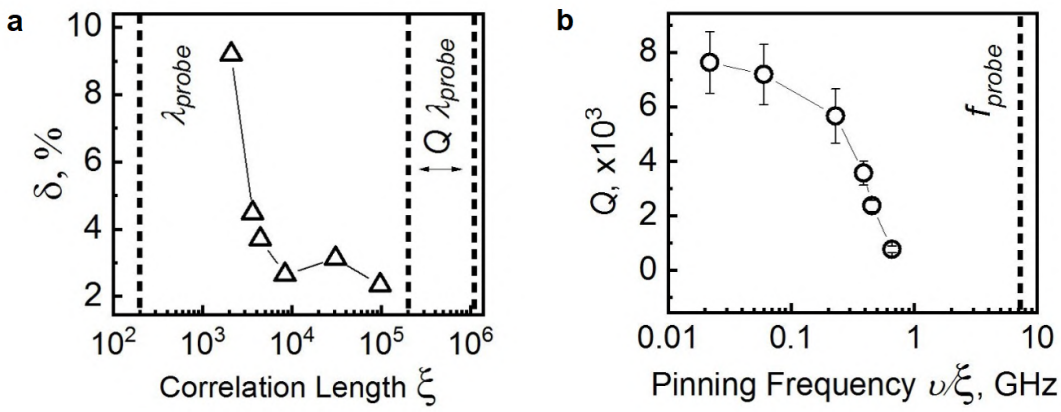

Figure 3.10: (a) The triangles are the r.m.s mode spacing fluctuation of a given device at a wavelength $\lambda_{\text{probe}} \approx 200$ unit cells, normalized by the average mode spacing. We plot their dependence vs. the theoretical correlation/pinning length ξ of the 1D Bose glass of the associated device. The product $Q\lambda_{\text{probe}}$ is the mean distance traversed by a collective mode photon of wavelength λ_{probe} and quality factor Q. Note that it exceeds the correlation/pinning length ξ. (b) Average quality factor at $\omega_{probe}/\omega_p \approx 0.35$ (corresponds to $f_{probe} \approx 7$ GHz) vs. theoretical pinning frequency v/ξ.

3.6 DC measurements and the role of transmission line length

We also conducted DC measurements on our devices. We used a standard lock-in technique with currents in range 1-10 pA. We found that the devices that had their internal quality factors trend to zero had a DC resistance in the megaohms. Furthermore some devices that had megaohm resistance did not show any novel decoherence at higher frequencies. The quality factors were shown to be length independent. However, the resistance is found to grow faster than the simple scaling due to length (Fig. 3.11).

The relevant length scale to compare to the coherence length is the wavelength of excitation. For DC measurements this is just the length of the device. For a given speed of light of our chain, changing the length of the device does not change the

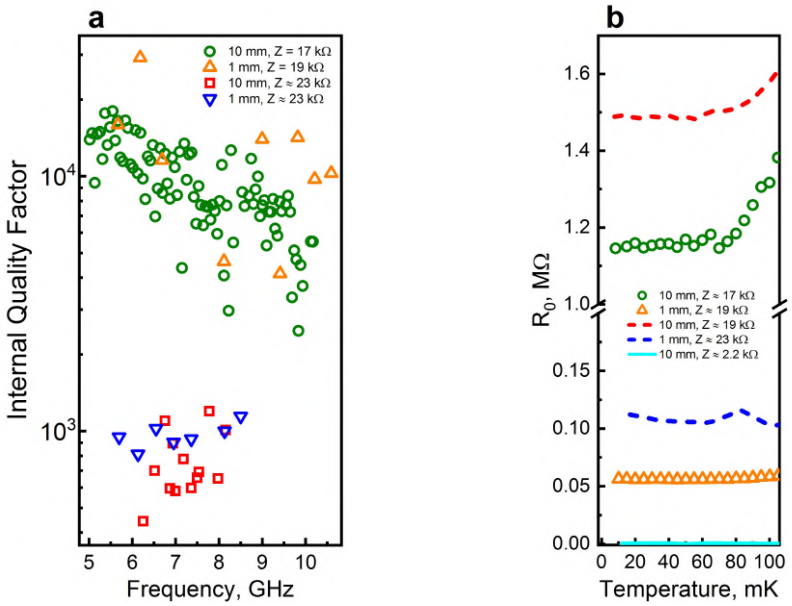

Figure 3.11: (a) Internal quality factor as a function of mode frequency measured for two pairs of nominally identical transmission lines but with the 10x difference in the length. (b) Zero-biased DC resistance as a function of temperature for several transmission lines of varying length and impedance.

wavelength at a given frequency. The mode index is changed but the wavelength is not. Thus a key advantage of using AC currents to investigate the insulating state is that it is insensitive to the length of the device. As predicted from theory [17] transport in the insulating state is highly dependent on temperature, frequency, and length. Given that any experiment is done with a device at finite temperature and length one needs more than a simple DC measurement to accurately identify the insulating state.

3.7 High-energy manifestations of quantum phase transitions

Our observations discussed in chapter 3 can be broadly interpreted as the high-energy view of a system near a quantum phase transition. All reported chains have parameters of an insulator in the conventional infrared limit. Yet, they behave

as superconductors when probed at wavelengths much shorter than the correlation (pinning) length ξ and at frequencies much higher than the pinning frequency ν/ξ (Fig. 3.10). Under such stimulus conditions, a disordered phase may be tricked into thinking that ξ is effectively infinite. Hence, it responds with a non-zero (but very low) phase stiffness throughout the entire system length—the necessary attribute of the ordered state. Importantly, the insulator leaves its footprint even in the high-energy limit, because the high-Q collective mode traverses distances far exceeding the correlation length. It consists of the small scatter (Fig. 3.10a) and broadening (Fig. 3.10b) of the collective mode resonances. These intrinsic interaction effects become visible when the values of $1/Q$ and δ outgrow the system-specific effects, such as dielectric loss and fabrication-induced disorder, respectively. We demonstrated this by either reducing ξ with weaker chains or by raising the excitation wavelength.

Decoherence of the phase mode in a 1D Bose glass has been explored theoretically in response to our experiment[25, 26, 27]. One mechanism is that a single probe photon decays into a large number of lower-frequency photons due to quantum phase slips [25, 26]. The other scenario describes the pinning of a charge density wave, which is a dual representation of the phase mode [27]. It causes an inhomogeneous broadening of the standing wave resonances after ensemble-averaging of their frequencies over disorder. This can indeed occur in a single device due to fluctuation of the offset charges in time. All models predict a scaling of $1/Q$ tied to the Bose glass quantum critical point in qualitative agreement with our measurement. More experimental, theoretical and numerical work is required to establish the quantitative scaling laws. The mode frequency scatter δ (Fig. 3.10a) remains unexplained.

Device	$v, 10^6$ m/sec	$\omega_p/2\pi$, GHz	Λ	Method 1 (Junction area) Z, kOhm	Method 1 (Junction area) E_J/E_C	Method 2 (Stripes capacitance) Z, kOhm	Method 2 (Stripes capacitance) E_J/E_C	ξ, unit cells	v/ξ, MHz
g	22.6	26.7	4.7	0.7	712	0.7	745	$--$	$-$
h	8.20	21.5	8.4	2.3	211	2.2	237	$--$	$-$
i	2.11	20.9	37.9	7.0	484	7.6	411	$\gg 10^6$	$\ll 1$
a	2.76	27.0	38.4	7.4	440	6.5	582	$\gg 10^6$	$\ll 1$
b	1.88	24.8	28.4	12.6	80	11.7	93	$\gg 10^6$	$\ll 1$
j	1.68	22.3	28.2	13.8	65	13.1	72	$\gg 10^6$	$\ll 1$
k	1.28	23.8	20.2	17.0	20.2	20.3	13.7	97815	22
c	1.12	20.8	20.2	19.0	15.8	23.1	10.2	31023	60
d	1.16	22.3	19.4	21.3	11.3	23.8	8.7	8399	230
l	1.04	20	19.4	23.1	9.3	26.6	6.7	4461	387
d'	0.99	19.3	19.3	23.6	8.7	27.8	5.9	3655	452
d''	1.12	21.6	19.4	21.8	10.6	24.7	8	6837	272
e	0.98*	20.8*	17.7*	23*	7*	29*	5*	2348	699
f	0.83*	20.8*	15*	19*	7*	22*	5*	2105	659

Table 3.1: Parameters for the Josephson transmission line devices. All lines are 10 mm long with the unit cell size $a = 0.6$ μm. The exceptions are devices g and h, where a is 40.2 μm and 10.2 μm respectively. The devices k, c, d, l, d' and f are used in the Fig.3.(7,9). $\Lambda = \sqrt{E_0/E_C}$ is the screening length of the charge-charge interaction inside our chains . The correlation (pinning) length ξ is found using the known device parameters as $\xi \approx (4E_0/W)^{2/(3-R_Q/Z)}$, where $W = 16/\sqrt{\pi}(8E_J^3E_C)^{1/4}\exp -\sqrt{8E_J/E_C}$.

These initial theories illustrate the advantage of the energy knob: by increasing the probe frequency, we effectively reduce the interactions in the renormalization group sense, and hence may keep the interaction-induced measurable quantities δ and 1/Q small, such that they can be calculated perturbatively. This could help to bridge theory and experiment of the SIT in a model BKT system. Our approach can be further extended to more complex SITs in thin superconducting films [48] and nanowires, where DC measurements left many fundamental questions unresolved [49] [50].

In chapter 4 we will obtain more insight about the photon decay process by studying the Josephson transmission line shunted by a single phase-slip junction.

Chapter 4: Inelastic scattering of photons on quantum phase slips

Although photons have zero mass, fundamental laws do not prevent their decay into more photons as soon as some form of non-linearity is present. Thus, individual 100 MeV-photons split in the Coulomb field of heavy nuclei because of vacuum polarization [51] and so do optical photons in non-linear crystals [52]. However, the splitting probability is extremely low, which in both cases can be traced down to the small value of the fine structure constant. Perhaps the strongest single-photon interaction effects occur in circuit quantum electrodynamics (cQED), owing to both the reduced mode volume of microwave transmission lines and the non-linearity of Josephson junctions [53]. Indeed, many basic quantum optical phenomena, such as vacuum Rabi oscillations [54], photon number splitting [55], resonance fluorescence [56], and parametric frequency conversion [57, 58], can be dramatically enhanced in properly designed superconducting circuits. In addition, multi-mode and ultrastrong coupling regimes were explored [59, 60, 61]. Yet, in the absence of a classical pump, the effect of one photon on another has been limited to a conditional phase-shift [62]. In this chapter, we describe the first instance of an inelastic photon-photon interaction, taking place in a massively multimode cavity resonator, and manifesting

as the rapid decay of a single microwave photon.

4.1 Device design

In chapter 4, the central part of our setup is a Josephson transmission line, as discussed in chapter 3, terminated by a weak Josephson junction made in the form of a symmetric SQUID (Fig. 1.3). The transmission lines we use have impedances Z of approximately 5 or 10 kΩ and have high enough E_J/E_C so that they are dielectric loss limited. They host the same modes as described previously and we use the same methods to measure them.

The SQUID at the end is composed of two small junctions of equal size which can be considered as a single "impurity" junction with flux-tunable Josephson energy $E_J(\Phi)$ and the charging energy E_C. The main difference between devices is the size of the SQUID junctions, or the values of E_C and $E_J(0)$. The SQUID loop area is kept constant throughout all devices.

4.2 Quantum phase-slip fluctuations as a virtual parametric pump

In the transmission line, microwave photons propagate as sound-like transverse electro-magnetic excitations of the superconducting phase field $\varphi(x,t)$ (Fig. 4.1). The impurity Josephson junction galvanically connected at $x = 0$ introduces two types of excitations into the phase field $\varphi(0,t)$ (Fig. 4.2). At the semi-classical level, the junction mimics a transmon qubit [63], whose resonance frequency $\omega_0 \approx \left((8E_JE_C)^{1/2} - E_C\right)/\hbar$ is associated with oscillations of $\varphi(x=0,t)$ inside a single

Josephson well. The resonance hybridizes with the transmission line modes and acquires a linewidth, given by the classical damping rate $\Gamma = 4E_C/\pi h\alpha$ [64]. Here, $\alpha = Z/R_Q$ is the effective fine structure constant, with Z being the impedance of the transmission line and $R_Q \approx 6.5$ kΩ being the resistance quantum for Cooper pairs.

The second effect on the phase field introduced by the weak junction is the 2π quantum phase slips at the rate $\lambda(\Phi)$. The quantum phase slips appear as a result of competing energy scales E_J and E_C. If E_J is much larger than E_C the phase is fixed. Alternatively if E_J is much smaller than E_C the charge is fixed. The regime we seek to address is between. Fluctuations of phase, as quantum phase slips, make the energy levels, which form the impurity resonance, sensitive to the dynamical charge q at the end of transmission line [23, 65, 66]. In contrast, any static charge is shunted by the large total capacitance of the transmission line. At small enough E_J/E_C the dynamical charge is not fixed and thus the energy level varies alongside it (Fig. 4.1, 4.2). As a result, incident photons experience a virtual parametric pumping of the impurity resonance by quantum fluctuations of q. As the "pump" strength, given by the phase-slip rate $\lambda(\Phi)$, grows, even a single photon can decay into an odd number of lower-frequency photons. This photon conversion is observed as an additional dissipation in our quality factor measurements (Fig. 4.3). By comparing the photon decay rates $2\pi\gamma = \omega/Q_{int}$ when the impurity is at different frequencies we can gain an image of its inelastic effect on the transmission line modes. When the impurity's resonance is at the plasma frequency, the impurity does not interact with the modes at frequencies from 4 to 10 GHz. We use this as our control for the background

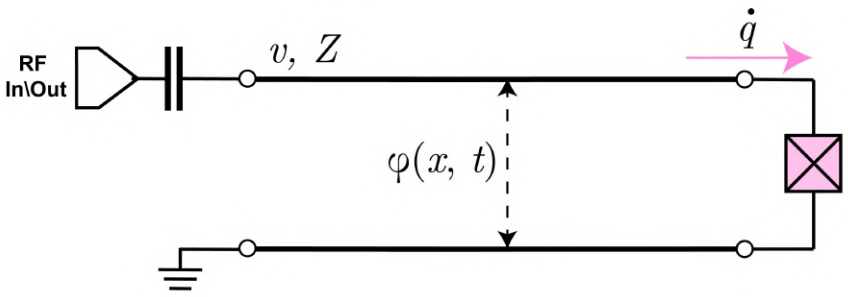

Figure 4.1: Circuit schematic of a telegraph transmission line terminated by a Josephson junction at the right end and weakly coupled to a measurement port at the left end. The quantum field $\varphi(x,t)$ represents the superconducting phase-difference between the two wires of the transmission line.

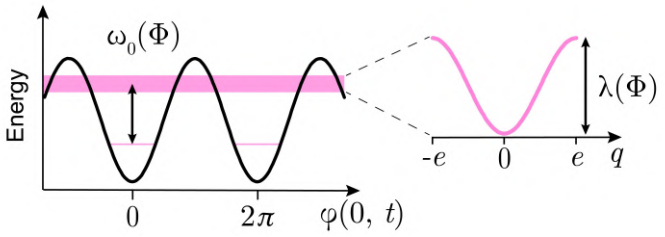

Figure 4.2: Quantum dynamics of the boundary phase ϕ(x = 0, t) in the periodic Josephson potential gives rise to a transmon-like resonance, whose frequency ω_0 is modulated by quantum fluctuations of the dynamical charge q at the end of the transmission line.

reflection excluding the effect of the impurity. The modes have the usual dielectric loss dependence and are spaced in frequency as normal transmission line modes. Then we tune the magnetic flux so the frequency of the impurity is within our range. The impurity is revealed by a shift in the frequencies of the modes centered at the frequency of the impurity. In addition we find that there is a peak in the inelastic loss rate centered at the frequency of the impurity. We measured many devices with different area junctions and saw qualitatively the same effect.

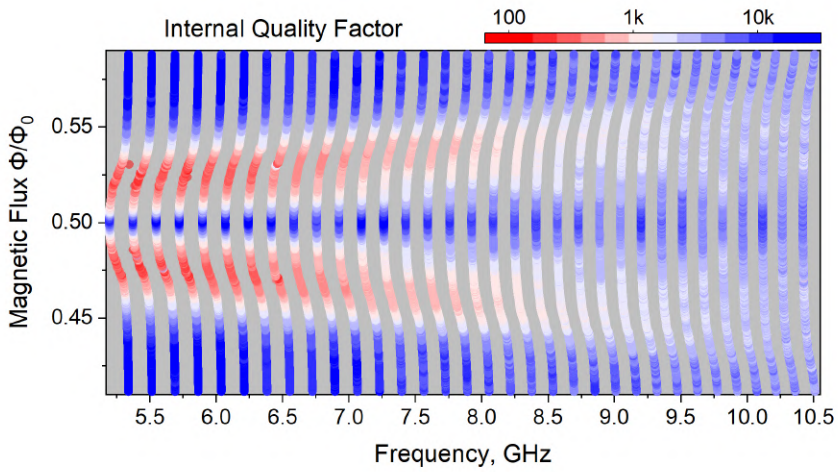

Figure 4.3: The measured positions of standing wave resonances as a function of flux through the impurity in device 3a. The color shows the resonances' internal quality factor.

4.3 Impurity-induced elastic and inelastic scattering

For a photon at frequency ω, the reflection off the impurity boundary contains elastic and inelastic contributions (Fig. 4.4). The elastic part appears in the form of the phase shift $\delta(\omega)$ acquired by the reflected photon. The elastic phase shift $\delta(\omega)$ is readily available as the shift in frequency, which the impurity induces on the transmission line modes, divided by the mode spacing Δ (Fig. 4.4 upper panels). The phase winds by π across the impurity resonance and provides the accurate measure of the impurity resonance linewidth Γ and, therefore, E_C.

Subtracting the background loss of each device from $\gamma(\omega)$, we interpret the remaining rate $\gamma_{\text{in}}(\omega)$ as the rate of photon decay due to inelastic scattering at the impurity. As we tune the impurity frequency the peak in the inelastic scattering rate shifts alongside it. In addition the peak height grows as the impurity frequency

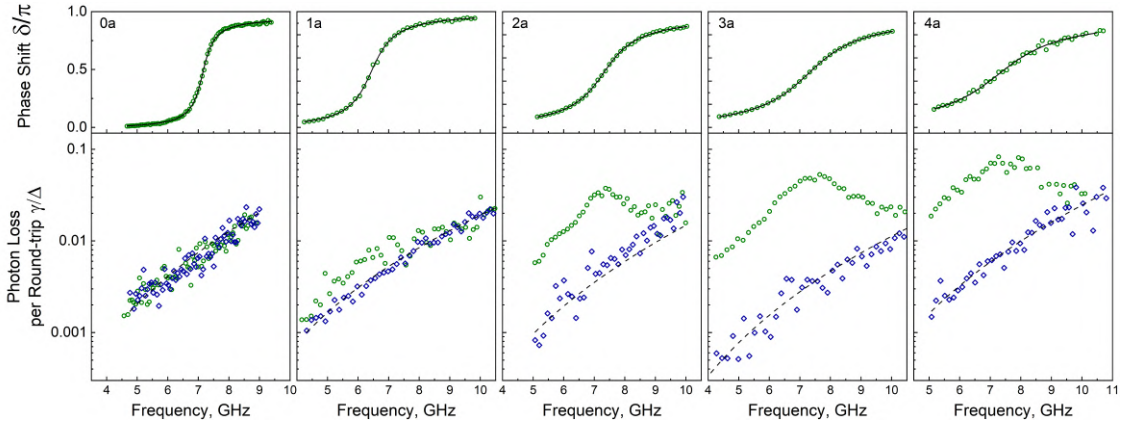

Figure 4.4: The elastic (top) and inelastic parts (bottom) of the reflection amplitude $r(\omega)$ for the devices with progressively larger charging energy E_C. In each device, the flux Φ is tuned such that $\omega_0/2\pi \approx 6.5 - 7.5$ GHz. The blue markers show data at $\Phi = 0$, where the impurity is effectively switched off. The dashed line represents the background dielectric loss inside the transmission line. Device parameters are given in the Table 4.1.

decreases, or effectively has a lower E_J/E_C due to the effective decrease in E_J (Fig. 4.4 lower panels).

The strong dependence of the inelastic scattering on the impurity's E_J/E_C is even more apparent in Figure 4.5. Such exponential growth is inconsistent with any material related loss like dielectric loss or quasiparticles induces loss. Moreover, the observed effect cannot be inhomogenous broadening due to flux noise as in device 1a which has the impurity frequency the most sensitive to flux we see no peak. Also, it cannot be due to coupling to the environment as external quality factor is unchanged with flux (Fig. 4.6). The observed decay rates can, however, be described using theory for photon decay due to quantum phase-slip fluctuations.

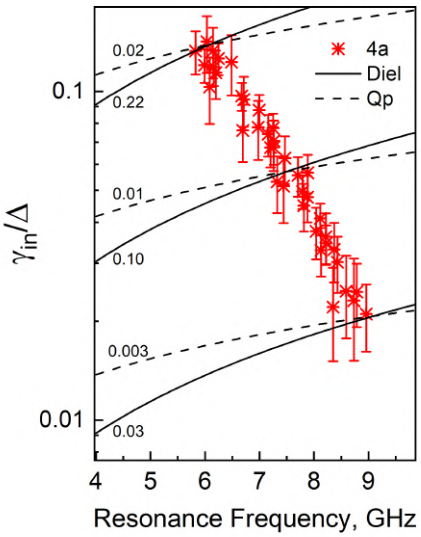

Figure 4.5: $\gamma_{\rm in}/\Delta$ at the resonance as a function of frequency (dots) and predictions for the dielectric loss (solid line) and quasiparticle induced loss (dashed line). Numbers near the theory lines indicate tan δ and x_{qp}.

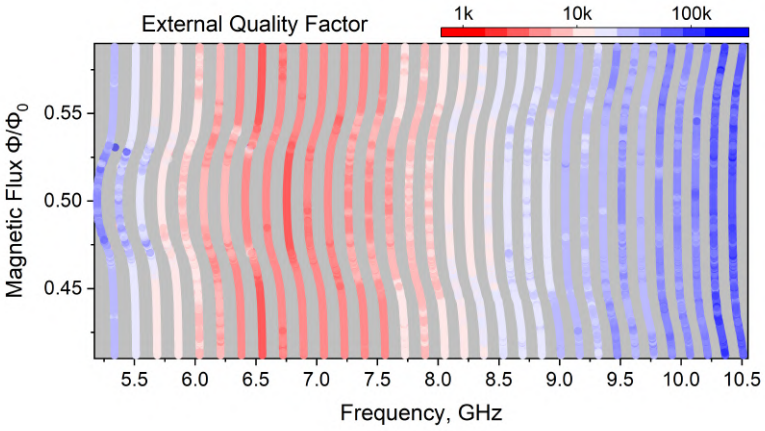

Figure 4.6: External quality factors as a function of frequency and external flux, controlled by a coil current. The strong frequency dependence of the Q_{ext} towards the lower frequencies is the result of the propagation cut-off of our copper waveguide at 7 GHz.

4.4 Theory versus experiment

Theory supports our interpretation of the anomalous dissipation in terms of photon decay[67, 68]. Specifically, for $\alpha > 1$, $\Gamma \ll \omega_0/2\pi$, and $E_C \ll E_J$, the observed photon decay can be quantitatively understood using the following effective phase-slip Hamiltonian,

$$H = \sum_k \hbar\omega_k a_k^\dagger a_k + \nu \cos \pi q/e. \tag{4.1}$$

The operators a_k ($a_k^\dagger$) annihilate (create) photons at flux-dependent frequencies ω_k, given by positions of the spectroscopic resonances (Fig. 4.3) and the effective phase-slip amplitude ν is proportional to the phase-slip rate $\lambda(\Phi)$ of the isolated junction. The dynamical charge q is decomposed over the normal modes according to $q = \sum_k f_k(a_k + a_k^\dagger)$, where the factors f_k weight the contribution of individual k-modes. The non-linearity of the cosine term in Eq. 4.1 creates a photon-photon interaction between all the k-modes at all even orders. According to Houzet et al. [67], the inelastic rate for a resonant photon can be found as:

$$\gamma_{in}(\omega = \omega_0)/\Delta = (\lambda/\omega_0)^2 \frac{(\pi\Gamma/\omega_0)^{2/\alpha-2}}{2(2/\alpha - 1)! \sin(\pi/\alpha)}. \tag{4.2}$$

Using this equation we compared its predictions to our experimental data for a number of different devices (Fig. 4.7). The inelastic scattering rate is highly dependant on the value of E_C for the impurity junction and this is highly sensitive to the certainty of knowing the experimental value of this parameter. The shaded

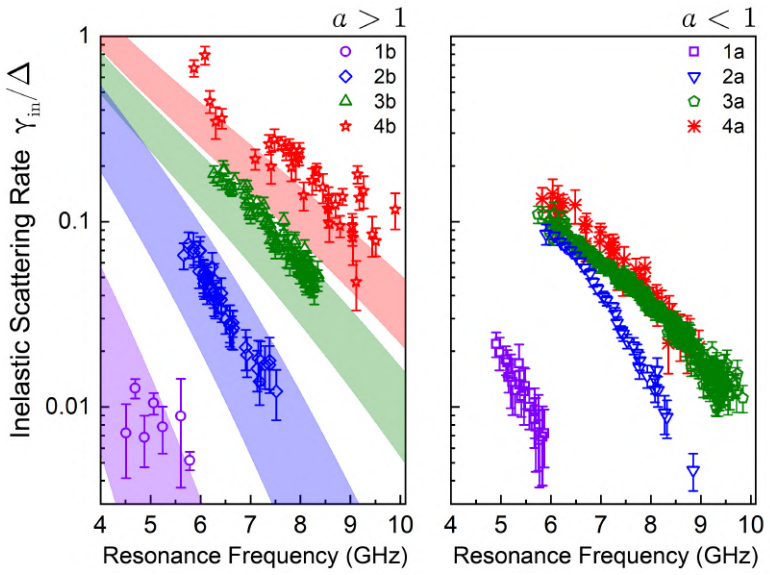

Figure 4.7: Inelastic scattering rate $\gamma_{\text{in}}(\omega_0)/\Delta$ (colored markers) for devices with $\alpha > 1$ (left panel) and $\alpha < 1$ (right panel). The width of theory lines (colored bands) comes from uncertainty in the device parameters. The error bars are the standard errors of $\gamma_{\text{in}}/\Delta$ at the resonance. The color code represents nominally identical values of E_C.

region gives the prediction for this range of uncertainty. We see broad agreement for the experimental data from all four devices with $\alpha > 1$. Also note that there are no fitting parameters in this model.

To gain further insight into the photon's lifetime, we consider specific final states available for the decay of mode 47 in device 3a, with flux Φ tuned such that $\omega_0/2\pi \approx \omega_{47}/2\pi \approx 6.476$ GHz. Using extended spectroscopy data (Fig. 4.8 left panel), we identified those three-photon and five-photon combinations, whose frequency matches $\omega_{47}/2\pi$ within the measured linewidth $\gamma = 11$ MHz. Our construction reveals a large number of states with a relatively uniform three-photon ($\Delta^{(3)} \approx 1$ MHz) and five-photon ($\Delta^{(5)} \approx 50$ kHz) level spacing (Fig. 4.8 right panel). States involving higher number of photons are also available and they would

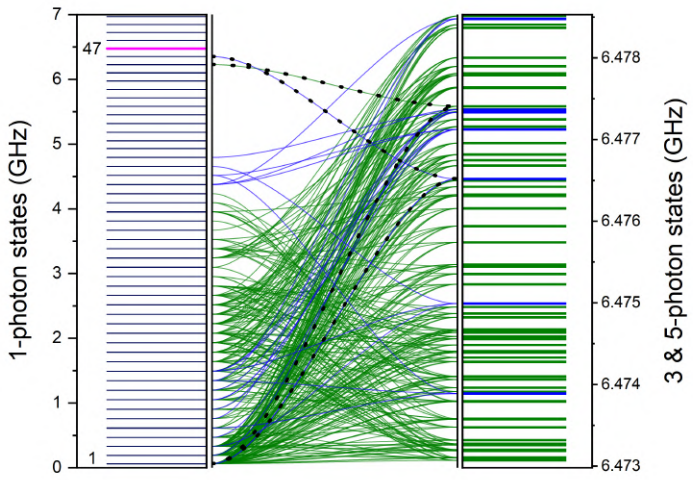

Figure 4.8: An example of the states available for the decay of the mode k = 47 in device 2a for $\omega_0 \approx \omega_{47}$. The many-body spectrum (right) is obtained by summing all possible combinations of three (blue) and five (green) one-photon frequencies, measured experimentally (left). The frequency range in the right panel equals to the measured half-linewidth of the k = 47 mode.

form even denser spectrum. The energy uniformity property comes from a small amount of disorder and dispersion in the single-particle spectrum, which breaks the otherwise massive degeneracy of multi-photon states.

The measured reflection coefficient is a non trivial many-body quantity that has been hard to obtain theoretically. The data collected that matches the theory give us confidence that our experiment accurately simulates the given Hamiltonian. However, we were also able to obtain data beyond the reach of current theory. This represents an useful analog quantum computation.

Device	v, 10^6 m/sec	$\omega_p/2\pi$, GHz	Δ, GHz	Z, $k\Omega$	α	Γ, GHz	E_C, GHz
0a	1.65	22.6	0.137	5.36 ± 0.67	0.83 ± 0.1	0.60 ± 0.02	0.39 ± 0.05
1a	1.93	23.0	0.161	5.26 ± 0.40	0.81 ± 0.06	1.03 ± 0.03	0.66 ± 0.05
2a	1.78	22.5	0.149	5.36 ± 0.05	0.83 ± 0.01	1.70 ± 0.02	1.11 ± 0.01
3a	2.25	27.3	0.188	4.44 ± 0.24	0.69 ± 0.04	2.50 ± 0.04	1.35 ± 0.08
4a	1.89	23.2	0.158	5.22 ± 0.21	0.81 ± 0.03	3.10 ± 0.09	1.96 ± 0.10
0b	1.99	24.5	0.166	9.82 ± 0.04	1.52 ± 0.01	0.32 ± 0.03	0.38 ± 0.03
1b	2.32	26.2	0.194	9.25 ± 1.16	1.43 ± 0.18	0.66 ± 0.02	0.74 ± 0.10
2b	1.37	17.5	0.114	13.61 ± 0.92	2.11 ± 0.14	0.63 ± 0.02	1.05 ± 0.08
3b	1.75	22.0	0.146	10.89 ± 0.42	1.68 ± 0.07	1.18 ± 0.04	1.56 ± 0.08
4b	1.72	21.0	0.143	11.38 ± 0.01	1.76 ± 0.00	1.32 ± 0.07	1.83 ± 0.10

Table 4.1: Parameters of devices with a single weak Josephson junction

Chapter 5: Conclusion and future directions

5.1 Conclusions

The main result of this thesis work is an observation of the effect of quantum phase-slip fluctuations on the phase mode in Josephson junction arrays. We started with a homogeneous array forming a telegraph transmission line where the superconductor to insulator quantum phase transition is expected. We showed that the phase mode survives far into the insulating regime, such that megaohm-resistance chains can carry gigahertz-frequency alternating currents as nearly ideal superconductors. The effect of quantum phase slips was found to result in the modes' broadening and increased frequency fluctuations of the collective mode resonances.

In order to better elucidate the role of the phase slips we constructed a system that isolates their effect to a single junction. Here we found that phase slip fluctuations can induce a decay of a single photon into multiple lower energy photons. Moreover localizing phase slips to a single junction allowed for a theoretical description that both qualitatively and quantitatively described the observed phenomena. Our observation of a single photon decay is the first reported example of light to light interaction at a single photon level.

For both the homogeneous arrays and the transmission lines shunted by a single

phase-slip junction, our measurement of the photon decay rates can be viewed as an analog quantum computation of a non-trivial many-body quantity. For the case of the single phase-slip junction, we successfully verified the computation outcome in the parameter regime available to analytical calculations. The rest of data represents a unique quantum resource for benchmarking numerical methods of many-body physics and testing noisy digital quantum computers.

One more outcome of this thesis work is the demonstration of a Josephson junction transmission line hosting a 1D electromagnetic mode with an effective fine structure constant exceeding unity, $\alpha > 1$. Systems with such a high constant are rare and this mode is a valuable resource for quantum science and technology. The availability of 1D microwave photons with impedance over 23 kΩ, demonstrated here, can transform many hybrid quantum platforms: from trapped polar molecules [69] and electrons on helium [70] to fabricated quantum dots [71], spin qubits [72] and nanomechanical systems [73].

5.2 Future directions

Our circuit spectroscopy technique can be readily extended to cover many quantum impurity models [74]. For instance, reducing the junction size (increasing E_C) would implement the boundary sine-Gordon (BSG) model [75, 76, 77]. The BSG model is notorious for its integrability property and for describing diverse condensed matter phenomena, from dissipative localization in a periodic potential [78, 79] to electron tunneling in Luttinger liquids [80]. Shunting the weak junction

by an inductance would implement a spin-boson model, related to Anderson and Kondo models[81, 82], in which case a large inelastic scattering cross-section was predicted near the Toulouse point [28]. Furthermore, rapidly switching the impurity on and off with the flux knob would induce controlled out-of-equilibrium dynamics.

The theoretical model for dissipation from the impurity had the photons being emitted into the lower frequency modes. Measurement of radiation being emitted from these modes would be an additional test of the theory. A potential complication is that the photons emitted at lower frequencies can continue to inelastically scatter to even lower frequencies. Thus, the intensity of the expected signal is hard to predict. If this signal could be seen it would reveal finer details of the decay process.

The possibility of inelastic scattering relied on having modes for the incoming light to scatter into. The chains we used were long enough such that there were plenty of combinations of lower mode frequencies within the linewidth of the measured mode. If this density were reduced by decreasing the length of the transmission line those combinations would disappear and thus so should the inelastic scattering. Understanding such energy localization transition in a nearly closed quantum system, originally introduced in the context of Fermi quasiparticles in a quantum dot [83], would be a timely extension of our experiment.

Finally, the presented in this thesis work experimental techniques promise a possible solution for a long standing problem of observation of the dissipative phase transition [78, 79]. Connected to a resistor, a single Josephson junction is expected to change its state from superconducting to insulating as the resistance value exceeds R_Q. This prediction can be tested with a circuit described in chapter 4, where a

Josephson junction transmission line implements an ohmic environment for a small Josephson junction connected to it. Importantly, the transmission line impedance can be in-situ tuned across the critical point at $Z = R_Q$ with the help of magnetic field. Whereas, the accurately measured phase of the reflected low frequency photons, as well as the photon decay data, provide unambiguous information about the nature of the small junction's ground state.

Appendix: A: Additional experimental methods

A.1 Heat tuning of the critical current density

When our junctions were heated up, we found that the inductance per junction decreased significantly in accordance with previous studies [84]. To heat we use a simple hot plate tuned to the desired temperature. The heating was done by placing the sample directly on a hot plate in a fume hood. We tested this procedure on a number of different resistance test devices (Tab. A.1). We found that this process was reproducible up to around 10 percent. The hotter the temperature the more the resistance decreased. In addition the temperature must be above 90 C to have a significant effect. This leads us to think that evaporation of water, which happens at 100 C, might be the cause for this effect. Increasing the amount of time heated past thirty minutes did not have much effect. Heating had a similar effect on junctions as on chains. Furthermore this effect persisted for many days after the heating.

A.2 Junctions made using dynamical oxidation

All our devices were made with passive oxidation. Here we flood the chamber with oxygen and then let the device sit in the oxygen. We also investigated a

Time Baked Baking Temperature	30 min 90 C	30 min 170 C	30 min 170 C	2 hr 170 C	4 hr 170 C	15 hr 170 C	30 min 300 C
20 Junction Chain 1	3%	55%	27%	58%	40%	40%	63%
20 Junction Chain 2	5%	13%	10%	48%	41%	38%	57%
100 Junction Chain 1	2%	52%	7%	58%	41%	37%	62%
100 Junction Chain 2	4%			49%	38%	40%	57%
Single small junction 1	5%	57%	37%	67%	49%	52%	70%
Single small junction 2	2%	33%	37%	59%	54%	48%	70%

Table A.1: Change in resistance due to heating. All values are in percent decrease from the resistance prior to heating. The chain junctions had area of 0.8 μm^2 while the single small junction had an area of 0.04 μm^2. Each sample had two 20 junction chains, 100 100 hundred junction chains and single small junctions to check reproducibility.

different way of forming the oxide, through dynamic oxidation. One motivation for this is the observation that the dielectric loss for our transmission lines is dependent on ω/ω_p. Thus if one increased the plasma frequency but kept the frequency the same the loss should be much lower.

In dynamic oxidation a steady stream of oxygen is sent over the sample. Previous attempts have found this procedure to work [36, 85]. Using an oxygen stream at 6 sccm for 10 minutes, we got junctions with resistances corresponding to plasma frequencies as high 200 GHz, much larger than any previously reported. These resistances were stable over time and repeatable. In fact the evidence from the small number of samples suggest it may be more repeatable than with static oxidation. Much more samples would need to be made to make any conclusion, but it is in correspondence with what was found in [36].

We also made a transmission line with junctions made using this technique. The inductance per junction found from its dispersion relation matches that of the resistance test experiments (Fig. A.1). Furthermore the quality factors we measured were higher. However, at some point above 30 GHz the dependence on ω/ω_p stopped

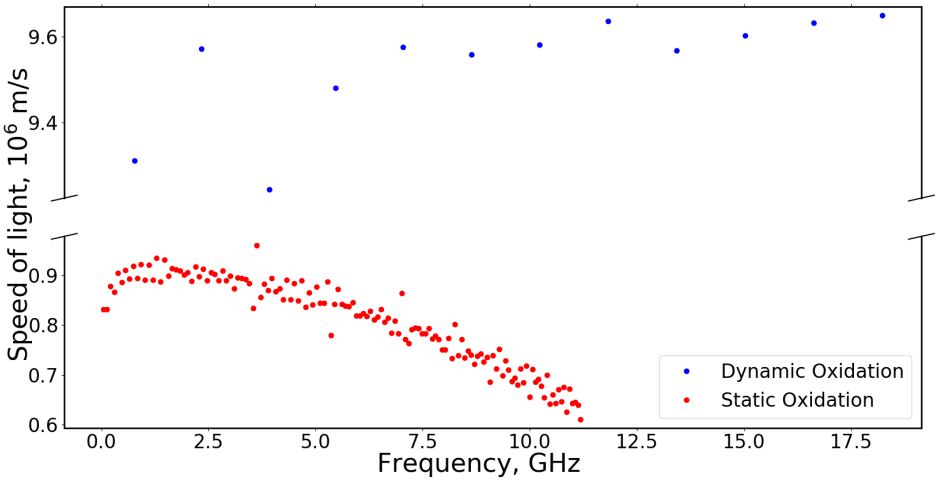

Figure A.1: The measured speed of light of a device made with dynamic oxidation compared to one with static oxidation. The speed of light is obtained from the mode spacing at each mode. The downward curve of the static oxidation is due to the bending from the plasma frequency. The lack of bending in the dynamic case confirms that the plasma frequency is much higher in this device.

and the quality factors plateaued. Perhaps some new loss mechanism arose that prevented the chains from realizing the gains predicted, but more investigations are needed to better understand what is going on.

Bibliography

[1] Sachdev, S. *Quantum Phase Transitions* (Cambridge University Press, 2011).

[2] Bradley, R. M. & Doniach, S. Quantum fluctuations in chains of Josephson junctions. *Phys. Rev. B* **30**, 1138–1147 (1984).

[3] Fazio, R., Wagenblast, K.-H., Winkelholz, C. & Schön, G. Tunneling into one-dimensional Josephson chains and Luttinger liquids. *Phys. B* **222**, 364–369 (1996).

[4] Basko, D. M. & Hekking, F. W. J. Disordered Josephson junction chains: Anderson localization of normal modes and impedance fluctuations. *Phys. Rev. B* **88**, 094507 (2013).

[5] Sondhi, S., Girvin, S., Carini, J. & Shahar, D. Continuous quantum phase transitions. *Rev. Mod. Phys.* **69**, 315–333 (1997).

[6] Kuzmin, R., Mencia, R., Grabon, N. *et al.* Quantum electrodynamics of a superconductor–insulator phase transition. *Nat. Phys.* **15**, 930–934 (2019).

[7] Kuzmin, R., Grabon, N. *et al.* Photon decay in circuit quantum electrodynamics. *Arxiv preprint arXiv:2010.02099* (2020).

[8] Josephson, B. D., 1962, *Phys. Lett.* **1**, 251.

[9] Tinkham, M. *Introduction to Superconductivity* (Courier Corporation, 1996).

[10] V. E. Manucharyan, J. Koch, L. I. Glazman, M. H. Devoret, *Science* **326**, 113 (2009).

[11] K. A. Matveev, A. I. Larkin, L. I. Glazman, Persistent current in superconducting nanorings. *Phys. Rev. Lett.* **89**, 096802 (2002).

[12] Berezinskii, V. L. Destruction of long-range order in one-dimensional and two-dimensional systems possessing a continuous symmetry group. II. Quantum systems. *Sov. Phys. JETP* **34**, 610–616 (1972)

[13] Kosterlitz, J. M. & Thouless, D. J. Ordering, metastability and phase-transitions in 2 dimensional systems. *J. Phys. C* **6**, 1181–1203 (1973)

[14] Korshunov, S. Effect of dissipation on the low-temperature properties of a tunnel-junction chain. *Zh. Eksp. Teor. Fiz.* **95**, 1058–1075 (1989).

[15] Choi, M.-S., Yi, J., Choi, M. Y., Choi, J. & Lee, S.-I. Quantum phase transitions in Josephson-junction chains. *Phys. Rev. B* **57**, 716–719 (1998).

[16] Giamarchi, T. Quantum Physics In One Dimension (Oxford University Press, 2004).

[17] Bard, M., Protopopov, I., Gornyi, I., Shnirman, A. & Mirlin, A. Superconductor–insulator transition in disordered Josephson-junction chains. *Phys. Rev. B* **96**, 064514 (2017).

[18] Cedergren, K. *et al.* Insulating Josephson junction chains as pinned Luttinger liquids. *Phys. Rev. Lett.* **119**, 167701 (2017).

[19] Giamarchi, T. & Schulz, H. J. Anderson localization and interactions in one-dimensional metals. *Phys. Rev. B* **37**, 325–340 (1988).

[20] Chow, E., Delsing, P. & Haviland, D. B. Length-scale dependence of the superconductor-to-insulator quantum phase transition in one dimension. *Phys. Rev. Lett.* **81**, 204–207 (1998).

[21] Haviland, D. B., Andersson, K. & Ågren, P. Superconducting and insulating behavior in one-dimensional Josephson junction arrays. *J. Low Temp. Phys.* **118**, 733–749 (2000).

[22] Ergül, A. *et al.* Localizing quantum phase slips in one-dimensional Josephson junction chains. *New J. Phys.* **15**, 095014 (2013).

[23] S. Corlevi, W. Guichard, F. W. J. Hekking, D. B. Haviland, Phase-charge

duality of a Josephson junction in a fluctuating electromagnetic environment. *Phys. Rev. Lett.* **97**, 096802 (2006).

[24] Lin, Y.-H., Nelson, J. & Goldman, A. M. Superconductivity of very thin films: the superconductor–insulator transition. *Phys. C* **514**, 130–141 (2015).

[25] M. Bard, I. Protopopov, A. Mirlin, Decay of plasmonic waves in Josephson junction chains. *Phys. Rev. B* **98**, 224513 (2018).

[26] H.-K. Wu, J. D. Sau, Theory of coherent phase modes in insulating Josephson junction chains. *Phys. Rev. B* **99**, 214509 (2019).

[27] M. Houzet, L. I. Glazman, Microwave spectroscopy of a weakly pinned charge density wave in a superinductor. *Phys. Rev. Lett.* **122**, 237701 (2019).

[28] M. Goldstein, M. H. Devoret, M. Houzet, L. I. Glazman, Inelastic microwave photon scattering off a quantum impurity in a Josephson-junction array. *Phys. Rev. Lett.* **110**, 017002 (2013).

[29] A. C. Hewson, *The Kondo Problem to Heavy Fermions* (Cambridge University Press, Cambridge, England, 1993).

[30] Kondo, J., 1964, *Prog. Theor. Phys.* **32**, 37.

[31] C. Wang, C. Axline, Y. Y. Gao, T. Brecht, Y. Chu, L. Frunzio, M.H. Devoret, and R.J. Schoelkopf, *Appl. Phys. Lett.* **107**, 162601 (2015).

[32] G. J. Dolan, "Offset masks for lift-off processing", *Appl. Phys Lett.*, vol. 31, pp. 337-339, 1977.

[33] L. Frunzio, A. Wallraff, D. Schuster, J. Majer, R. Schoelkopf, *Applied Superconductivity, IEEE Transactions on* **15**, 860 (2005).

[34] V. Ambegaokar and A. Baratoff, *Phys. Rev. Lett.* **10**, 486 (1963); **11**, 104 (1963).

[35] C. D. Nugroho, V. Orlyanchik, and D. J. Van Harlingen, *Appl. Phys. Lett.* **102**, 142602 (2013).

[36] Kreikebaum, J. M., O'Brien, K. P., Morvan, A. & Siddiqi, I. Improving wafer-scale Josephson junction resistance variation in superconducting quantum coherent circuits.

[37] I. M. Pop *et al.*, *J. Vac. Sci. Technol., B* **30**, 010607 (2012).

[38] M.D. Hutchings, J.B. Hertzberg, Y. Liu, N.T. Bronn, G.A. Keefe, M. Brink, J.M. Chow, and B.L.T. Plourde, Tunable Superconducting Qubits with Flux-Independent Coherence, *Phys. Rev. Applied* **8**, 044003 (2017).

[39] Devoret, M. H. Quantum fluctuations in electrical circuits. In *Fluctuations Quantiques/Quantum Fluctuations: Les Houches Session LXIII* (ed. Reynaud, S. et al.) 351–386 (Elsevier, 1997).

[40] Weißl, T. *et al.* Kerr coefficients of plasma resonances in Josephson junction chains. *Phys. Rev. B* **92**, 104508 (2015).

[41] K. C. Gupta, R. Garg, I. Bahl, and P. Bhartia, *Microstrip Lines and Slotlines* (Arttech House, Inc., Norwood, MA, 1996).

[42] Choi, M.-S., Choi, M., Choi, T. & Lee, S.-I. Cotunneling transport and quantum phase transitions in coupled Josephson-junction chains with charge frustration. *Phys. Rev. Lett.* **81**, 4240–4243 (1998).

[43] Haus, H. A. *Electromagnetic Noise and Quantum Optical Measurements* 84-88 (Advanced Texts in Physics, Springer, 2000)

[44] Gunnarsson, D. *et al.* Dielectric losses in multi-layer Josephson junction qubits. *Supercond. Sci. Technol.* **26**, 085010 (2013).

[45] G. Rastelli, I. M. Pop, F. W. J. Hekking, Quantum phase slips in Josephson junction rings. *Phys. Rev. B* **87**, 174513 (2013).

[46] Fukuyama, H. & Lee, P. A. Dynamics of the charge-density wave. I. Impurity pinning in a single chain. *Phys. Rev. B* **17**, 535–541 (1978).

[47] Vogt, N. *et al.* One-dimensional Josephson junction arrays: lifting the Coulomb blockade by depinning. *Phys. Rev. B* **92**, 045435 (2015).

[48] Crane, R. *et al.* Survival of superconducting correlations across the two-dimensional superconductor–insulator transition: a finite-frequency study. Phys. Rev. B 75, 184530 (2007).

[49] Arutyunov, K. Y., Golubev, D. S. & Zaikin, A. D. Superconductivity in one dimension. *Phys. Rep.* **464**, 1–70 (2008).

[50] Sacépé, B. *et al.* Localization of preformed Cooper pairs in disordered superconductors. *Nat. Phys.* **7**, 239–244 (2011).

[51] S. Z. Akhmadaliev, *et al.*, Experimental investigation of high-energy photon splitting in atomic fields. *Phys. Rev.Lett.* **89**, 061802 (2002).

[52] T. Guerreiro, *et al.*, Nonlinear interaction between single photons. *Phys. Rev. Lett.* **113**, 173601 (2014).

[53] A. Blais, S. M. Girvin, W. D. Oliver, Quantum information processing and quantum optics with circuit quantum electrodynamics. *Nat. Phys.* **16**, 247 (2020).

[54] A. Wallraff, *et al.*, Strong coupling of a single photon to a superconducting qubit using circuit quantum electrodynamics. *Nature* **431**, 162 (2004).

[55] D. Schuster, *et al.*, Resolving photon number states in a superconducting circuit. *Nature* **445**, 515 (2007).

[56] O. Astafiev, *et al.*, Resonance fluorescence of a single artificial atom. *Science* **327**, 840 (2010).

[57] N. Bergeal, *et al.*, Analog information processing at the quantum limit with a Josephson ring modulator. *Nat.Phys.* **6**, 296 (2010).

[58] C. S. Chang, *et al.*, Observation of three-photon spontaneous parametric down-conversion in a superconducting parametric cavity. *Phys. Rev. X* **10**, 011011 (2020).

[59] N. M. Sundaresan, *et al.*, Beyond strong coupling in a multimode cavity. *Phys. Rev. X* **5**, 021035 (2015).

[60] P. Forn-Díaz, L. Lamata, E. Rico, J. Kono, E. Solano, Ultrastrong coupling regimes of light-matter interaction. *Rev. Mod. Phys.* **91**, 025005 (2019).

[61] A. F. Kockum, A. Miranowicz, S. De Liberato, S. Savasta, F. Nori, Ultrastrong coupling between light and matter. *Nat Rev Phys* **1**, 19 (2019).

[62] S. E. Nigg, *et al.*, Black-box superconducting circuit quantization. *Phys. Rev. Lett.* **108**, 240502 (2012).

[63] J. Koch, *et al.*, Charge-insensitive qubit design derived from the Cooper pair box. *Phys. Rev. A* **76**, 042319 (2007).

[64] R. Kuzmin, N. Mehta, N. Grabon, R. Mencia, V. E. Manucharyan, Superstrong coupling in circuit quantum electrodynamics. *npj Quantum Inf* **5**, 20 (2019).

[65] I. V. Pechenezhskiy, R. A. Mencia, L. B. Nguyen, Y.- H. Lin, V. E. Manucharyan, The superconducting quasicharge qubit. *Nature*, in press (2020).

[66] D. V. Averin, A. B. Zorin, K. K. Likharev, Bloch oscillations in small Josephson junctions. *Sov. Phys. JETP* **61**, 407 (1985).

[67] M. Houzet and L. I. Glazman, In preparation, (2020).

[68] A. Burshtein, *Arxiv preprint arXiv:2010.02630* (2020).

[69] André, A. *et al.* A coherent all-electrical interface between polar molecules and mesoscopic superconducting resonators. *Nat. Phys.* **2**, 636–642 (2006).

[70] Schuster, D., Fragner, A., Dykman, M., Lyon, S. & Schoelkopf, R. Proposal for manipulating and detecting spin and orbital states of trapped electrons on helium using cavity quantum electrodynamics. *Phys. Rev. Lett.* **105**, 040503 (2010).

[71] Stockklauser, A. *et al.* Strong coupling cavity QED with gate-defined double

quantum dots enabled by a high impedance resonator. *Phys. Rev. X* **7**, 011030 (2017).

[72] Samkharadze, N. *et al.* Strong spin–photon coupling in silicon. *Science* **359**, 1123–1127 (2018).

[73] Arrangoiz-Arriola, P. *et al.* Coupling a superconducting quantum circuit to a phononic crystal defect cavity. *Phys. Rev. X* **8**, 031007 (2018).

[74] E. Gull, *et al.*, Continuous-time monte carlo methods for quantum impurity models. *Rev. Mod. Phys.* **83**, 349 (2011).

[75] A. O. Gogolin, A. A. Nersesyan, A. M. Tsvelik, *Bosonization and strongly correlated systems* (Cambridge University Press, 2004).

[76] A. Roy, *et al.*, *Arxiv preprint arXiv:2007.06874* (2020).

[77] P. Fendley, H. Saleur, N. P. Warner, Exact solution of a massless scalar field with a relevant boundary interaction. *Nucl. Phys. B* **430**, 577 (1994).

[78] A. Schmid, Diffusion and localization in a dissipative quantum system. *Phys. Rev. Lett.* **51**, 1506 (1983).

[79] S. Bulgadaev, Phase diagram of a dissipative quantum system. *Pis'ma v Zh. Eksp. Teor. Fiz.* **39**, 264 (1984).

[80] C. L. Kane, M. P. A. Fisher, Transport in a one-channel luttinger liquid. *Phys. Rev. Lett.* **68**, 1220 (1992).

[81] J. J. García-Ripoll, E. Solano, M. A. Martin-Delgado, Quantum simulation of anderson and kondo lattices with superconducting qubits. *Phys. Rev. B* **77**, 024522 (2008).

[82] K. Le Hur, Kondo resonance of a microwave photon. *Phys. Rev. B* **85**, 140506 (2012).

[83] B. L. Altshuler, Y. Gefen, A. Kamenev, L. S. Levitov, Quasiparticle lifetime in a finite system: A nonperturbative approach. *Phys. Rev. Lett.* **78**, 2803 (1997).

Supercond. Sci. Technol. **33**, 06LT02 (2020).

[84] Jared Hertzberg, *et al.*, *Arxiv preprint arXiv:2009.00781* (2020).

[85] Y.-L. Wu, H. Deng, H.-F. Yu, G.-M. Xue, Y. Tian, J. Li, Y.-F. Chen, S.-P. Zhao, and D.-N. Zheng, *Chin. Phys. B* **22**, 060309 (2013).